

Fractured Geothermal Reservoir Using CO₂ as Geofluid: Numerical Analysis and Machine Learning Modeling

Published as part of ACS Omega virtual special issue “CO₂ Geostorage”.

Manojkumar Gudala, Zeeshan Tariq,* Suresh Kumar Govindarajan, Bicheng Yan,* and Shuyu Sun*



Cite This: *ACS Omega* 2024, 9, 7746–7769



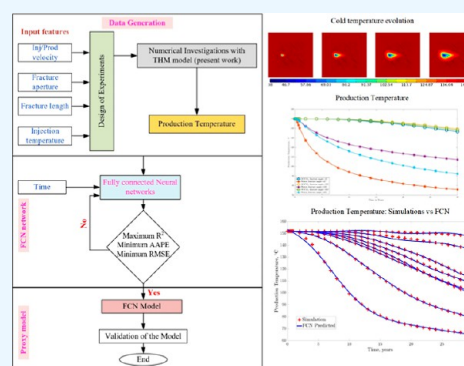
Read Online

ACCESS |

Metrics & More

Article Recommendations

ABSTRACT: The effect of natural fractures, their orientation, and their interaction with hydraulic fractures on the extraction of heat and the extension of injection fluid are fully examined. A fully coupled and dynamic thermo-hydro-mechanical (THM) model is utilized to examine the behavior of a fractured geothermal reservoir with supercritical CO₂ as a geofluid. The interaction between natural fracture and hydraulic fracture, as well as the type and location of geofluids, influences the production temperature, thermal strain, mechanical strains, and effective stress in rock/fractures in the reservoir. A mathematical model is developed by using the fully connected neural network (FCN) model to establish a mathematical relationship between the reservoir parameters and the temperature. The response surface methodology is applied for qualitative numerical experimentation. It is found that the developed FCN model can be utilized to forecast the temporal variation of temperature in the production well to a desired level using FCN. Therefore, the numerical simulations developed with the FCN method can be useful tools to investigate the temperature evolution with higher accuracy.



INTRODUCTION

Geothermal energy is renewable in nature and abundant in the crust of the Earth. Geothermal reservoirs can be classified as hydrothermal and hot dry rock (HDR) geothermal reservoirs. HDR geothermal reservoirs have low porosity and permeability and are generally available at a depth of 3 to 10 km from the surface. As the heat stored in the HDR cannot be extracted via conventional engineering techniques, proper selection of injection and production wells connected by hydraulic fractures in high-temperature regions is required, namely, engineered/enhanced geothermal systems (EGS).^{1,2}

Cold fluid or heat transfer medium (geofluid), e.g., water or other working fluid, is injected into EGS to extract the heat energy from the earth's crust to the surface. Recently, supercritical CO₂ (SCCO₂) has gained a lot of attention as an alternative geofluid for the extraction of heat from geothermal reservoirs. As first mentioned by Brown,³ SCCO₂ as a geofluid is considered superior to water due to its high compressibility, high expansivity, and low viscosity. As a result, there is less resistance for transport of SCCO₂ in permeable rocks and fractures, helping to reduce the injection pump power and engineering cost. Previous numerical studies in geothermal reservoirs^{4–18} have also shown that SCCO₂ performed better as a geofluid than water. Biagi et al. (2015) investigated the extraction of heat from the geothermal reservoir using CO₂ as geofluid.⁴ They used the TOUGH2 module ECO2N simulator to simulate thermal

variation. They found that the decline in the production temperature is due to the cooling of the rock matrix. Zhang et al. (2016) investigated the performance of CO₂ as a geofluid during the organic Rankine cycle (ORC) operation in the geothermal reservoir.⁵ They found that the quality of CO₂ and the production temperature influenced the selection of the ORC fluid. They also found that the efficiency of the CO₂-EGS systems decreases with impurities in CO₂. Pan et al. (2016) investigated the feasibility of (SCCO₂) as a geofluid using a thermohydro model.⁶ They found that (SCCO₂) outperforms the Acoculco, Puruáñdiro, and Agua Caliente Comond reservoirs of Mexico. It is about 160% more than the water-based systems. Zhang et al. (2017) studied the extraction of geothermal heat from high temperature gas reservoirs using CO₂ as a geofluid.⁷ They also investigated the geological storage of CO₂ in the high-temperature gas reservoirs. They found that the quality of CO₂ produced from the high-temperature gas reservoir greatly influences the geothermal performance. A low

Received: September 20, 2023

Revised: January 4, 2024

Accepted: January 8, 2024

Published: February 6, 2024



Table 1. Comparison of the Present THM Model with the Existing Models Using CO₂ as a Geofluid

SI. no	author	geofluid	type of model	remarks	ML/DL/NN
1	Biagi et al. (2015) ⁴	CO ₂ and water	TH	no mechanical model which overestimates the production temperature	no
2	Zhang et al. (2016) ⁵	CO ₂ and water	TH for ORC	no mechanical model which overestimates the production temperature	no
3	Pan et al. (2016) ⁶	CO ₂ and water	TH	no mechanical model which overestimates the production temperature	no
4	Zhang et al. (2017) ⁷	CO ₂ and natural gas	two-phase TH	no mechanical model which overestimates the production temperature	no
5	Pan et al. (2015) ⁸	CO ₂ and water	TH wellbore model	no mechanical model which overestimates the production temperature	no
6	Yin et al. (2011) ¹⁰	CO ₂ and water	THMC	not much effect of the chemical process during the geothermal operation is identified and computationally very expensive	no
7	Zhang et al. (2013) ¹¹	CO ₂ and water	TH	no mechanical model which overestimates the production temperature	no
8	Liang et al. (2016) ¹³	CO ₂ and water	TH	no mechanical model which overestimates the production temperature	no
9	Luo et al. (2014) ¹⁶	CO ₂ and water	TH	no mechanical model which overestimates the production temperature	no
10	Wang et al. (2018) ¹⁷	CO ₂ and water	TH	the no mechanical model which overestimates the production temperature	no
11	Guo et al. (2019) ¹⁸	CO ₂ and water	TH	no mechanical model which overestimates the production temperature	no
12	Yan et al. (2023) ⁵⁵	water	THM model	single fracture and hot sedimentary aquifers	yes
13	Yan et al. (2023) ⁵⁶	water	THM model	single fracture	yes
14	Zhou et al. (2019) ¹	water	TH model	no mechanical model which overestimates the production temperature	yes
15	Pandey et al. (2021) ⁵⁷	water	TH model	the no mechanical model which overestimates the production temperature	yes
16	present work	CO ₂ and water	THM model with dynamic rock, fluid, and fracture properties	assumed no chemical reactions occur during the operation of heating recovery from the geothermal reservoir; multi fracture system	yes

water and methane content will improve the geothermal efficiency of the high-temperature gas reservoirs. Pan et al. (2015) developed a well-reservoir model for geothermal reservoirs using CO₂ as a geofluid.⁸ Yin et al. (2011) developed a finite element code to inject CO₂ into porous media.¹⁰ They investigated the pressure and stress variations near the well during the injection of CO₂ and found that temperature and chemical effects influence high pressure and stress, leading to reservoir injection problems. Zhang et al. (2013) investigated the thermodynamic performance of CO₂-EGS over water-EGS.¹¹ They found that CO₂-EGS systems produce more heat than water-EGS systems in low-enthalpy reservoirs. CO₂-EGS systems are underperforming at high flow rates due to high resistance losses. Liang et al. (2016) investigated the geothermal performance using CO₂ as a geofluid.¹³ Their study divided the process into three stages: 100% water production, water-CO₂ coproduction stage, and only CO₂ production stage. They found that geochemical reactions had less impact on the heat performance of the reservoir. From their investigation, 45% of the heat recovered from the reservoir. They also suggested that a proper selection reservoir is essential to implement this technology. Luo et al. (2014) numerically investigated the performance of CO₂-EGS systems in a geothermal reservoir with doublet configuration.¹⁶ CO₂ injection rates can influence heat transfer between the fluid and the rock matrix. The production temperature is reduced with an increasing mass injection rate. They found that a mass flow rate of 10 kg/s is the most favorable for 20 years of heat mining using CO₂ as a geofluid in double systems. Wang et al. (2018) found that the CO₂ systems have more fluid loss than the water system during heat extraction.¹⁷ They found an increase in formation permeability in CO₂-based

systems, which increases the level of sequestration of CO₂ in geothermal reservoirs. Guo et al. (2019) investigated the performance of a fractured geothermal reservoir using CO₂ as a geofluid.¹⁸ They found that an increase in the density of the fractures decreases the heat extraction rate. They found that the systems based on CO₂ perform well for a given flow rate compared with those based on water from fractured geothermal systems. Furthermore, the evolution of the CO₂ plume in the reservoirs during geothermal recovery also led to the excellent capacity of geological CO₂ sequestration.^{4–9} The mathematical models used in the above works do not consider the dynamic variation of rock and fracture properties. Therefore, in the present work, we focus on developing the THM model with dynamic variation of fluid, rock, and fracture properties.

In enhanced geothermal systems (EGS), hydraulics and natural fractures play a significant role in heat production and fluid flow. When cold fluid is injected into the reservoir through injection wells, it becomes hotter during transportation and is ultimately produced as hot fluid from the production wells.^{15,18–23} Natural and hydraulic fractures have better transmissibility than the rock matrix and thus act as preferential fluid flow paths.^{2,15,17,19–25} Therefore, the recovery of heat from hot dry rocks is based mainly on the distribution of natural and hydraulic fractures.^{26–28} The evolution of the flow and mechanical force fields in the geothermal reservoir depends mainly on the external loads imposed and the thermal drag,^{26–29} which can generate stress and strain due to thermal and mechanical variations in the reservoir. Fractures' permeability changes during cold water circulation, resulting from variations in thermal stresses.^{30–33} These variations impact the effective normal stress in the fracture, causing it to open and then close.

As the fluid continues to circulate, the temperature in the vicinity of the fractures decreases, altering the effective stress and causing the fracture to close slightly, thus maintaining dynamic behavior.^{33,34} These variations caused dynamic fluid flow in fractures, so the type of geofluid and lateral forces are critical during heat extraction.

The use of data-driven models, particularly deep learning (DL) models, in the energy sector has increased rapidly because of their predictive capabilities. These models are capable of handling nonlinear problems of high dimensions, which is more efficient than traditional numerical simulations based on physics.^{35–40} DL has been used in various applications, such as predicting rock properties, reservoir fluid properties, production performance, well testing, geological CO₂ sequestration, and production temperature in geothermal reservoirs.^{36–38,41–54} Recently, DNNs have been used to predict the production temperature at different time steps in geothermal reservoir modeling. Yan et al. (2023) developed a robust general thermal decline model for geothermal reservoirs. They integrated it with DL and Multi-Objective Optimization for geothermal reservoir management considering uncertainties in reservoir property.⁵⁵ Yan et al. (2023) used the Fourier neural operator to predict the geothermal temperature field over time with a heterogeneous fracture aperture field in EGS with high precision and further performed reservoir optimization for temperature control based on a control neural network (NN) or stochastic gradient descent method.⁵⁶ Zhou et al. (2019) developed a NN model based on backpropagation to predict the production temperature of the Zhacang geothermal reservoir.¹ They used the TOUGH2-EOS1 code, a thermo-hydro model, to generate a data set for training and testing. The R^2 of the ANN-based model is 0.998 for training and 0.98 for testing. Pandey et al. (2021) developed an artificial NN model for thermal drawdown in the EGS system.⁵⁷ This work created a data set with a thermo-hydro model using the local temperature, pressure, mass rate, and fracture transmissibility. Kalogirou et al. (2021) developed thermal maps at three different depths such as 20, 50, and 100 m using artificial NNs.⁵⁸ Esen and Inalli (2009) used the ANN model to predict the performance of vertical ground-coupled heat pumps for cooling and heating cycles. In this work, the vertical well bore is used to extract heat from the three different depths, including 30, 60, and 90 m, and found that the Levenberg–Marquardt backpropagation algorithm with 8 neurons is best suitable for both predicting cooling and heating cycles.⁵⁹ Gudmundsdottir and Horne (2020) used the feedforward model (MLP) and recurrent neural network (RNN) models to predict tracer concentrations in the production well to investigate the breakthrough in the synthetic fractured reservoir. They found that the MLP model performed better and faster in training compared to the RNN model.⁶⁰ Akin et al. (2010) used artificial intelligence techniques to optimize well locations in the Kizildere geothermal field in Türkiye. They used five mass rates to optimize well distances in this field.⁶¹ The comparison of the different models used in geothermal reservoirs with CO₂ as geofluid and the application of different ML/DL/NN models are presented in Table 1.

Motivated by previous work, this research focuses mainly on developing the THM model with dynamic properties. Utilization of SCCO₂ as a geofluid during the heat extraction operation is compared with the water-EGS system. The physical and thermal properties of CO₂ are a function of the pressure and temperature. Which is actually used in the present work. Injection of cold fluid into the fractured reservoir leads to rapid

cooling and variation in rock and fracture parameters. These variations are included in the developed mathematical model. We evaluate the impact of the orientation of natural fractures and its interaction with hydraulic fractures. Furthermore, we develop a hybrid predictive approach involving fully connected neural network (FCN) models to establish a mathematical relationship between the influencing parameters and the production temperature. The response surface methodology (RSM) is utilized to quantify the number of qualitative numerical experiments required to establish FCN models. These models are trained using data from the physics simulations. They can be used to predict the production temperature of proposed scenarios within the maximum and minimum limits of the primary control parameters, including injection temperature, injection and production velocities, aperture, and length of the HF. We also present the mathematical relation between the input and output variables in the present work.

The communication is organized as follows. In the **Mathematical Modeling Section**, we introduce the governing equations for heat transfer, fluid flow, and geomechanics for porous media and fractures. In the **Geological Model for the Heat Extraction from Geothermal Reservoir Section**, we provide information on the geometry of the computational model, the creation of fractures in the porous medium, and the initial and boundary conditions. The implementation of the governing equations, coupled equations, is presented in the **THM Model Implementation Section**. In the **Results and Discussion Section**, we provide results and discussions of temperature variation and strain variations along with the selection of NNs to predict the temporal evolution of the production temperature. Finally, we conclude this work with a few remarks in the **Conclusions Section**.

MATHEMATICAL MODELING

Mathematical Equations. The mathematical formulations used in this study, which relate the transportation of heat and fluid in a rock matrix with geomechanical variations, are given by eqs 1–24. The transfer of heat in the rock matrix is presented in eq 1.

$$(\rho C_p)_{\text{eff}} \frac{\partial T}{\partial t} + \rho_{\text{fl}} C_{p,\text{fl}} u_{\text{dlm}} \cdot \nabla T - \nabla \cdot (\lambda_{\text{eff}} \nabla T) = Q_{\text{m,frac}} \quad (1)$$

$$(\rho C_p)_{\text{eff}} = \phi_{\text{mat}} \rho_{\text{mat}} C_{p,\text{mat}} + (1 - \phi_{\text{mat}}) \rho_{\text{fl}} C_{p,\text{fl}} \quad (2)$$

$$\lambda_{\text{eff}} = \phi_{\text{mat}} \lambda_{\text{mat}} + (1 - \phi_{\text{mat}}) \lambda_{\text{fl}} \quad (3)$$

$$u_{\text{dlm}} = \frac{\kappa_{\text{mat}}}{\mu_{\text{fl}}} \nabla p_{\text{m}} \quad (4)$$

Here, $(\rho C_p)_{\text{eff}}$ is the effective heat capacity within the matrix; ϕ_{mat} is the rock porosity; ρ_{mat} is the rock density; $C_{p,\text{mat}}$ is the heat capacity of the matrix; $C_{p,\text{fl}}$ is the heat capacity of the fluid; λ_{eff} is the effective thermal conductivity within the matrix; λ_{mat} is the thermal conductivity of the matrix; λ_{fl} is the thermal conductivity of the fluid; $Q_{\text{m,frac}}$ is the coupled source/sink term, which accounts for the heat transfer from matrix to fracture and fracture to matrix; u_{dlm} is the Darcy velocity; p is the pressure, T is the temperature.

The collective mass conservation and momentum equation⁶² is presented in eq 5.

$$\frac{(\partial\phi_{\text{mat}}\rho_{\text{fl}})}{\partial t} + \nabla \cdot (\rho_{\text{fl}}u_{\text{dlm}}) - q_{\text{m}} = 0 \quad (5)$$

In eq 5, q_{m} accounts for the mechanical variations that occur during fluid flow in the matrix. The mathematical representation of q_{m} is given in eq 6.

$$q_{\text{m}} = \rho_{\text{fl}} \left(1 - \frac{K_{\text{d}}}{K_{\text{fl}}} \right) \frac{\partial \varepsilon_{\text{vol}}}{\partial t} \quad (6)$$

The mathematical equation that can represent the poroelastic storage is given in eq 7

$$\frac{(\partial\phi_{\text{mat}}\rho_{\text{fl}})}{\partial t} = \frac{\rho_{\text{fl}}}{M} \frac{\partial p}{\partial t} \quad (7)$$

The Biot's modulus (M) and Biot–Willis coefficient (α_{b}) are given in eqs 8 and 9, respectively.^{63,64}

$$\frac{1}{M} = \frac{\phi_{\text{mat}}}{K_{\text{fl}}} + (\alpha_{\text{b}} - \phi_{\text{mat}}) \frac{1 - \phi_{\text{mat}}}{K_{\text{d}}} \quad (8)$$

$$\alpha_{\text{b}} = 1 - \frac{K_{\text{d}}}{K_{\text{fl}}} \quad (9)$$

Here, α_{b} is the Biot–Willis coefficient; K_{d} and K_{fl} are the drain modulus and fluid modulus, respectively. A simplified form of the combined hydro-mechanical equation is given in eq 10.

$$\begin{aligned} \rho_{\text{fl}} \left[\frac{\phi_{\text{mat}}}{K_{\text{fl}}} + \left(1 - \frac{K_{\text{d}}}{K_{\text{fl}}} - \phi_{\text{mat}} \right) \frac{1 - \phi_{\text{mat}}}{K_{\text{d}}} \right] \frac{\partial p_{\text{m}}}{\partial t} - \nabla \cdot (\rho_{\text{fl}}u_{\text{dlm}}) \\ = \rho_{\text{fl}} \left(1 - \frac{K_{\text{d}}}{K_{\text{fl}}} \right) \frac{\partial \varepsilon_{\text{vol}}}{\partial t} \end{aligned} \quad (10)$$

The heat transfer in the natural/hydraulic fractures is represented in eq 11.

$$\begin{aligned} d_{\text{afrc}}(\rho C_p)_{\text{eff}} \frac{\partial T}{\partial t} + d_{\text{afrc}}(\rho_{\text{fl}} C_{p,\text{fl}})_{\text{frc}} u_{\text{frc}} \cdot \nabla T - \nabla \\ \cdot (d_{\text{afrc}}(\lambda_{\text{eff}})_{\text{frc}} \nabla T) \\ = d_{\text{afrc}} Q_{\text{m,fracT}} \end{aligned} \quad (11)$$

The governing equation to describe the fluid flow with mechanical variations in the fracture is given in eq 12.

$$d_{\text{f}} \frac{\partial \phi_{\text{f}} \rho_{\text{w}}}{\partial t} + \nabla_{\text{Tn}} \cdot (\rho_{\text{w}} d_{\text{f}} u_{\text{f}}) = d_{\text{f}} \rho_{\text{w}} \alpha_{\text{b}} \frac{\partial \varepsilon_{\text{V}}}{\partial t} + d_{\text{f}} q_{\text{f}} \quad (12)$$

The flow rate (u_{f}) per unit length in the natural or hydraulic fractures is given by eq 13.

$$u_{\text{f}} = - \frac{d_{\text{f}}^2}{12R_{\text{f}}\mu_{\text{w}}} \nabla_{\text{Tn}} p_{\text{f}} \quad (13)$$

The mass transfer coupling (that is, q_{f}) between the rock matrix and the fracture is shown in eq 14.

$$q_{\text{f}} = - \frac{\kappa_{\text{f}}}{\mu_{\text{w}}} \frac{\partial p}{\partial n} \quad (14)$$

The volumetric strain (ε_{vol}) is described in eq 15.

$$\varepsilon_{\text{vol}} = \varepsilon_{11} + \varepsilon_{22} \quad (15)$$

The displacement vectors, ε_{11} and ε_{22} , in eq 15 are defined as follows: $\varepsilon_{\text{ab}} = 0.5 \left(\frac{\partial u_{\text{da}}}{\partial x_{\text{b}}} + \frac{\partial u_{\text{db}}}{\partial x_{\text{a}}} \right)$, where u_{da} and u_{db} are the

displacement vectors in the “a” and “b” directions, respectively. The governing equation for the equilibrium of forces acting on the computational domain is presented in eq 16.^{65–69}

$$\nabla \cdot \left[\sigma_{\text{s}} - \alpha_{\text{b}} p_{\text{m}} - \varepsilon_{\text{T}} \left(\frac{E}{1 - 2\eta} \right) \right] + (\rho_{\text{fl}} \phi_{\text{mat}} + \rho_{\text{mat}}) = F_{\text{A}} \quad (16)$$

Here, σ_{s} is the stress, E is the elastic modulus, and η is the Poisons ratio. Natural and hydraulic fractures in the computational domain are considered thin elastic layers in the present work. The force per unit area acting on the fracture is mathematically represented as a function of the spring constant (k_{A}), damping constant per unit area (d_{A}), and the thickness of the fracture (or the aperture of the fracture) (d_{afrc}), which gives the following eq 21.

The fractures in this work are considered to be a thin elastic layer. The force per unit area acting on the fracture mathematically represented as a function of the spring constant ($k_{\text{A},\text{f}}$), damping constant per unit area ($d_{\text{A},\text{f}}$), and fracture thickness (or fracture aperture) (d_{f}) is given in the following eq 17.

$$\begin{aligned} F_{\text{A},\text{f}} = -k_{\text{A},\text{f}}(u_{\text{u},\text{f}} - u_{\text{d},\text{f}} - u_0) - d_{\text{A},\text{f}} \frac{\partial(u_{\text{u},\text{f}} - u_{\text{d},\text{f}} - u_0)}{\partial t} \\ - 0.5\rho_{\text{f}} d_{\text{f}} \frac{\partial^2(u_{\text{u},\text{f}} + u_{\text{d},\text{f}})}{\partial t^2} \end{aligned} \quad (17)$$

The spring constant for the unit area acting on the thin elastic layer is described in eq 18.

$$k_{\text{A}} = k_{\text{n},\text{f}} n \otimes n + k_{\text{s},\text{f}} (I - n \otimes n) \quad (18)$$

The stiffness of the fracture ($k_{\text{n},\text{f}}$) in the normal direction and the shear stiffness of the fracture ($k_{\text{s},\text{f}}$) are defined as a function of the elastic modulus and the Poisson ratios of the fractures given in the eqs 23 and 24, respectively.

$$k_{\text{n},\text{f}} = \frac{E_{\text{f}}(1 - \nu_{\text{f}})}{d_{\text{f}}(1 + \nu_{\text{f}})(1 - 2\nu_{\text{f}})} \quad (19)$$

$$k_{\text{s},\text{f}} = \frac{E_{\text{f}}}{2d_{\text{f}}(1 + \nu_{\text{f}})} \quad (20)$$

$$\begin{aligned} F_{\text{A}} = -K_{\text{A}}(u_{\text{u}} - u_{\text{d}} - u_0) - d_{\text{A}} \frac{\partial(u_{\text{u}} - u_{\text{d}} - u_0)}{\partial t} \\ - 0.5\rho_{\text{mat}} d_{\text{afrc}} \frac{\partial^2(u_{\text{u}} + u_{\text{d}})}{\partial t^2} \end{aligned} \quad (21)$$

The spring constant for the unit area is given in eq 22

$$k_{\text{A}} = k_{\text{n}} n \otimes n + k_{\text{s}} (I - n \otimes n) \quad (22)$$

The stiffness in the normal direction and the shear stiffness are defined as a function of both the elastic modulus, and the Poisson ratios of fractures are given in eqs 23 and 24, respectively.

$$k_{\text{n}} = \frac{E_{\text{frc}}(1 - \nu_{\text{frc}})}{d_{\text{afrc}}(1 + \nu_{\text{frc}})(1 - 2\nu_{\text{frc}})} \quad (23)$$

$$k_{\text{s}} = \frac{E_{\text{frc}}}{2d_{\text{afrc}}(1 + \nu_{\text{frc}})} \quad (24)$$

Rock, Fracture, and Fluid Properties. The porosity of the rock matrix used in the present work depends on the variation of

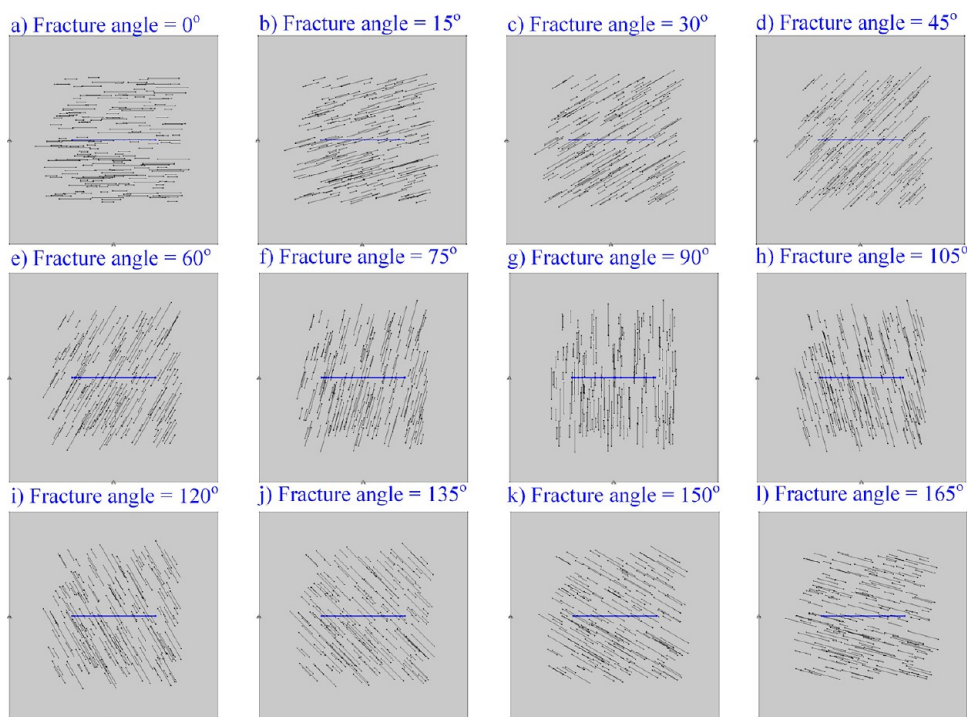


Figure 1. Arrangement of natural fracture in the porous media (Fracture aperture varied from 0.1 to 5 mm and fracture length varied from 1 to 40 m).

strains generated due to mechanical and thermal loads and is given in eq 25.^{66,70}

$$\begin{aligned}\phi_{\text{mat}} &= \frac{\phi_{\text{ini}} + \Delta\epsilon_{\text{vol}} - \Delta\epsilon_{\text{T}}}{1 + \Delta\epsilon_{\text{vol}}} \\ &= \frac{\phi_{\text{ini}} + \Delta\epsilon_{\text{vol}} - [\alpha_{\text{T}}(1 - \phi_{\text{ini}})\Delta T]}{1 + \Delta\epsilon_{\text{vol}}}\end{aligned}\quad (25)$$

The elastic modulus of the rock and fractures is a function of the porosity variation (i.e., eq 25) and is represented in eq 26.⁷¹

$$\ln\left(\frac{E}{E_i}\right) = -d(\phi_{\text{mat}} - \phi_{\text{ini}})\quad (26)$$

The variation in permeability of the rock matrix and fractures is represented in the equations (27) and (28), respectively.^{72–74}

$$\ln\left(\frac{\kappa}{\kappa_0}\right) = \left[\frac{(1 - \phi_{\text{ini}})a_1 + b_1\phi_{\text{ini}}}{\phi_{\text{ini}}}\right]\epsilon_{\text{vol}} = C_n\epsilon_{\text{vol}}\quad (27)$$

$$\kappa_{\text{frCN}} = \kappa_{\text{frCO}} \exp\left(\frac{-\sigma_n}{\sigma^*}\right)\quad (28)$$

The heat capacity and thermal conductivity of the rock and fracture are given in eqs 29 and 30 respectively.^{50,66}

$$C_{p,\text{mat}}(\kappa) = \left[\frac{(2.6\log(\kappa) + 4.2) \times 10^3}{2.7\log(\kappa) + 0.3}; \right. \\ \left. \text{if } -20 \leq \log(\kappa) \leq -11 \right]$$

$$C_{p,\text{mat}}(\kappa) = [-13\log(\kappa) + 699; \\ \text{if } -11 \leq \log(\kappa) \leq -2]\quad (29)$$

$$\lambda_r(T) = 2.6 - 0.0025(T - 293.15)\quad (30)$$

The effect of temperature variation on water viscosity, water density, water specific heat, and water thermal conductivity is expressed in mathematical equations, namely eqs 31, 32, 33, and 34, respectively.^{72,75}

$$\mu_w(T) = \begin{cases} 1.38 - 0.028T + 1.36 \times 10^{-4}T^2 \\ - 4.61 \times 10^{-7}T^3 + 8.9 \times 10^{-10}T^4 \\ - 9.08 \times 10^{-13}T^5 \\ + 3.84 \times 10^{-16}T^6; \\ \text{if } 273.15 \leq T \leq 413.15 \\ 0.004 - 2.11 \times 10^{-5}T + 3.86 \times 10^{-8}T^2 \\ + 2.4 \times 10^{-11}T^3; \\ \text{if } 413.15 \leq T \leq 553.15 \end{cases}\quad (31)$$

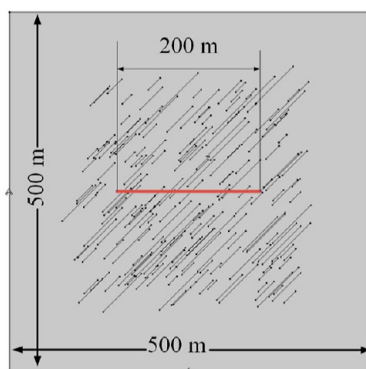
$$\rho_w(T) = 838.47 + 1.4T - 0.003T^2 + 3.72 \times 10^{-7}T^3\quad (32)$$

$$C_{pw}(T) = 12010.15 - 80.41T + 0.31T^2 - 5.38 \times 10^{-4}T^3 \\ + 3.62 \times 10^{-7}T^4\quad (33)$$

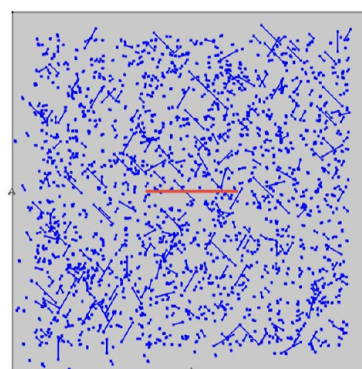
$$\lambda_w(T) = -0.869 + 0.009T - 1.58 \times 10^{-5}T^2 \\ + 7.98 \times 10^{-9}T^3\quad (34)$$

Variations in the thermodynamic properties of SCCO₂, including viscosity, density, heat capacity, and thermal conductivity, are described in eqs 35–38. These properties depend on temperature and pressure and are valid within the temperature range of 273 to 553 K and the pressure range of 15 to 40 MPa.¹⁵

a) Reservoir geometry



b) Complex Reservoir geometry



c) Boundary conditions

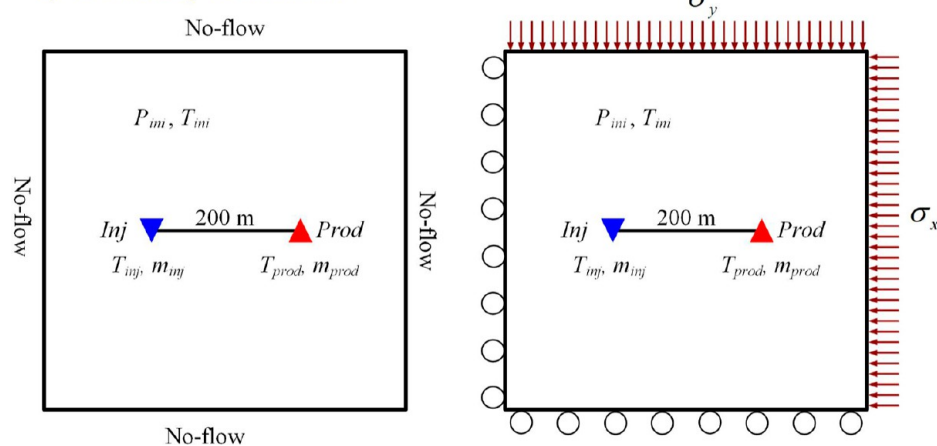


Figure 2. Reservoir geometry and boundary conditions.

$$\begin{aligned} \mu_{\text{SCCO}_2}(T, p) = & 7.14 \times 10^{-9}T^2 + 5.642 \times 10^{-6}T \\ & - 5.71 \times 10^{-9}p^2 + 2.186 \times 10^{-6}p \\ & + 0.0011 \end{aligned} \quad (35)$$

$$\begin{aligned} \rho_{\text{SCCO}_2}(T, p) = & 0.00036T^3 - 0.3693T^2 + 122T \\ & - 0.333p^2 + 32.54p - 12720 \end{aligned} \quad (36)$$

$$\begin{aligned} C_{p,\text{SCCO}_2}(T, p) = & -4.9 \times 10^{-5}T^3 + 0.084T^2 - 49.11T \\ & - 0.47p^3 - 42.1p^2 + 1200p + 276.3 \end{aligned} \quad (37)$$

$$\begin{aligned} \lambda_{\text{SCCO}_2}(T, p) = & -1.75 \times 10^{-8}T^3 + 2.29 \times 10^{-5}T^2 \\ & - 0.01T - 1.89 \times 10^{-5}p^3 + 0.0007p^2 \\ & - 0.006p + 1.46 \end{aligned} \quad (38)$$

■ GEOLOGICAL MODEL FOR THE HEAT EXTRACTION FROM GEOTHERMAL RESERVOIR

Computational Model. In this work, we use a two-dimensional (2D) porous media geometry with dimensions of $500 \times 500 \times 30 \text{ m}^3$ x - y - z directions. There is a 200 m long hydraulic fracture, as shown in Figures 1 and 2a. The cold fluid injection and heat production wells are placed at the extremes of the hydraulic fracture, the primary flow path for the geofluid to

gain heat from the surrounding rock. The computational porous domain has an initial rock porosity of 0.04 and an initial rock permeability of $3.2 \times 10^{-16} \text{ m}^2$. Natural fractures vary in length from 5 to 40 m, and their orientations change from 0 to 165° , as shown in Figure 1. Figure 2b shows the complex reservoir geometry with different arrangements of the natural fractures.

Natural Fracture Geometry. The generation of natural fractures is discussed in detail in this section. The development of an appropriate fracture network^{76–78} in porous media is essential to characterize fluid flow, especially in the development of EGS, because the fracture network dominates the extraction of heat from the rock as the geofluid moves from the injection well to the production well.^{2,24,79} We adopt the power-law distribution function to generate natural fractures in the computational domain. The mathematical representation of the power-law distribution is presented in eq 39.

$$f(a) = \frac{b-1}{a_{\min}} \left(\frac{a}{a_{\min}} \right)^{-b} \quad (39)$$

where a is the population value; a_{\min} is the minimum population value; b is the power law exponent.

The Fisher distribution is used to define the orientation of the fracture. The mathematical form of the Fisher distribution is described as follows,

$$f(\theta) = K_F \frac{\sin \theta e^{K_F \cos \theta}}{e^{K_F} - e^{-K_F}} \quad (40)$$

Table 2. Rock, Fracture, and Fluid Properties^{75,81–83}

property	rock properties	fluid properties
density, kg/m ³	2600	eq 32
dynamic viscosity, Pa.s		eq 31
thermal conductivity, W/m.K	eq 30	eq 34
heat capacity at constant pressure, J/kg.K	eq 29	eq 33
coefficient of thermal expansion, K ⁻¹	3×10^{-5}	
initial Young's modulus, GPa	24	
Poisson's ratio	0.26	
initial porosity	0.03	
initial permeability, m ²	3.2×10^{-16}	
ratio of specific heats		1.0
Biot–Willis coefficient	0.25–0.75	
fluid-injection rate, m/s		0.1
fluid-production rate, m/s		0.1
initial reservoir temperature, °C	180	
fluid injection temperature, °C		20
initial Young's modulus-fracture, GPa	2.4	
Poisson's ratio-fracture	0.104	
fracture aperture, mm	0.2	
fracture porosity	1	
boundary load: x-direction, MPa	48	
boundary load: y-direction, MPa	44	

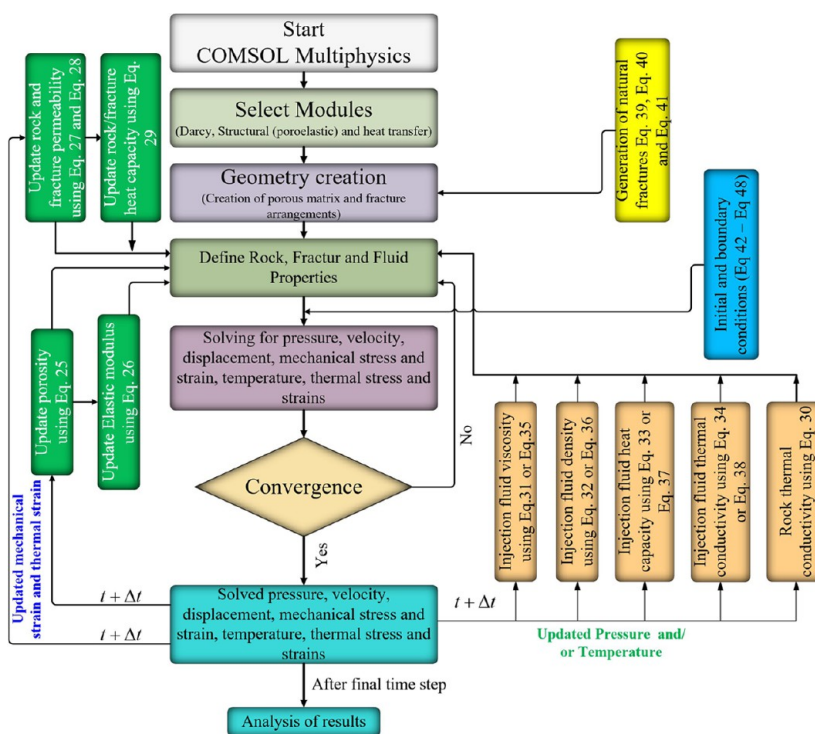


Figure 3. Schematic of the solution process employed for fully coupled thermohydrmechanical model in the present work.

In eq 40, K_F is the Fisher constant; θ is the angular deviation of the fracture. Fisher constant (K_F) indicates the tightness of the orientation cluster. The aperture, orientation, and distribution of the fractures strongly determine the flow characteristics of the natural fractures. In general, the walls of natural fractures are rough. In the present work, we consider the walls to be smooth.⁸⁰ The aperture is uniformly distributed from 0.1 to 5 mm. The relation between the length of the fracture and the aperture of the fracture is given in eq 41.

$$d_{\text{afc}} = c_{\text{pf}} \cdot l_{\text{fc}} \quad (41)$$

where c_{pf} is a proportionality factor; l_{fc} is the length of fracture; d_{afc} is the aperture of the fracture.

Initial and Boundary Conditions. The initial temperature of the geothermal reservoir is 425 K (151.85 °C) with an average reservoir pressure of 15 MPa. The porous domain is appropriate to confine the effects of boundaries during the extraction of heat from the rock matrix. Thus, constant temperatures equal to the initial reservoir temperature are maintained at the boundaries. No-flow conditions are employed for fluid flow at the reservoir boundaries. In the geomechanical section, the rolling and lateral stresses (i.e., σ_x and σ_y) are applied to two boundaries, as shown

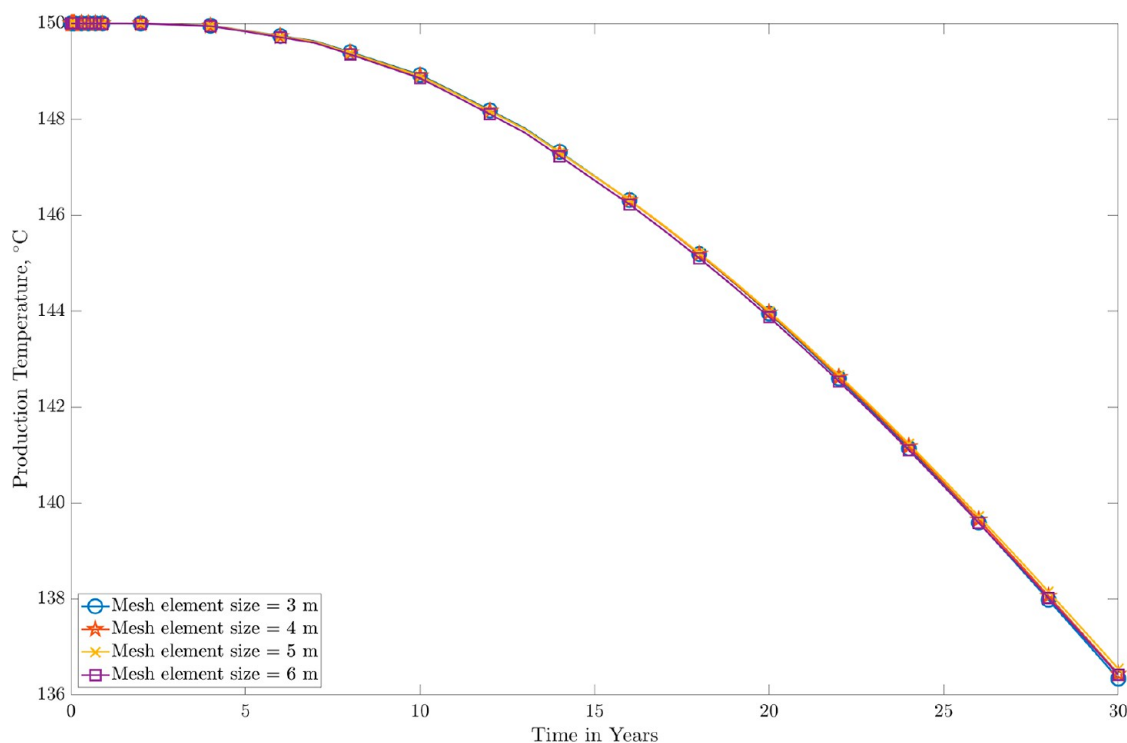


Figure 4. Mesh sensitivity studies the production temperature.

in Figure 2c. The properties of the rock, fracture, and injected fluid are listed in Table 2. The initial conditions for the fluid flow, temperature, and displacement fields are provided in eqs 42, 43, 44, and 45, respectively.

$$p(x, y, t)_{t=0} = p_{\text{ini}} \quad (42)$$

$$T(x, y, t)_{t=0} = T_{\text{ini}} \quad (43)$$

$$[u_x, u_y]_{t=0}^T = [0, 0]^T \quad (44)$$

$$\left[\frac{\partial u_x}{\partial t}, \frac{\partial u_y}{\partial t} \right]_{t=0}^T = [0, 0]^T \quad (45)$$

The fluid flow boundary conditions at the injection well and the production well are represented by eqs 46 and 47, respectively.

$$\text{At injection well: } m(t)_{\text{inj}} = u_{\text{inj}} \rho_w / \text{SCCO}_2 \quad (46)$$

$$\text{At production well: } m(t)_{\text{prod}} = u_{\text{inj}} \rho_w / \text{SCCO}_2 \quad (47)$$

The heat flux boundary condition is used at the injection well and is given in eq 48.

$$\begin{aligned} \text{At injection well: } q(t)_{\text{inj}} \\ = C_{p,w/\text{SCCO}_2} (T_{\text{inj}} - T_0) u_{\text{inj}} \rho_w / \text{SCCO}_2 \end{aligned} \quad (48)$$

THM Model Implementation. COMSOL Multiphysics is a finite element simulator, and engineers utilize COMSOL Multiphysics to perform fully coupled numerical investigations for geothermal reservoirs.^{69,84–92} In this work, we utilize heat transfer, poroelasticity, Darcy flow, solid mechanics, and thermal expansion modules integrated with COMSOL Multiphysics and develop a fully coupled and dynamic THM model for the geothermal reservoir with natural and hydraulic fractures

(Figure 3). Coupled interactions, presented as local variables in the component section, are embedded (i.e., eqs 25–38). In the solid mechanics module, natural and hydraulic fractures are designated as a thin elastic layer, and the mathematical formulation is presented from eqs 21–24. The fracture flow physics conditions are used to model fluid and heat flow in the fractures in both Darcy's law and heat transfer modules. The developed THM model is implemented in fully coupled mode. The dynamic variables (i.e., presented in Section Rock, Fracture, and Fluid Properties) are implemented in the COMSOL multiphysics as local variables. The model updates these variables for each time step based on the variations in pressure and temperature in the rock and fracture. Sequentially, stationary and transient solvers are employed. The backward difference formula with the Euler backward initialization technique is used, and the multifrontal massively parallel sparse direct linear solver is utilized to solve pressure and displacement. Furthermore, a parallel direct sparse solver is used for solving the temperature.

Mesh Sensitivity. In numerical modeling, mesh sensitivity analysis is significant because it helps establish the lowest mesh density that is adequate to offer a reliable and accurate solution to the problem being modeled. This helps to ensure that the model is as precise and reliable as possible. If the mesh is too coarse, the solution may be erroneous and unreliable, but if the mesh is too fine, it may lead to larger computation times and an increase in the required processing resources. In the work presented here, we use unstructured grids. The sensitivity of the grid to production temperature is studied and presented in Figure 4. The production temperature is consistent until the mesh size is 5 m. When the element size increases to 6 m, an underestimation of the production temperature is observed. The results are consistent and accurate until the mesh size is 5 m. So, in the present work, we use the element size of 5 m for each model.

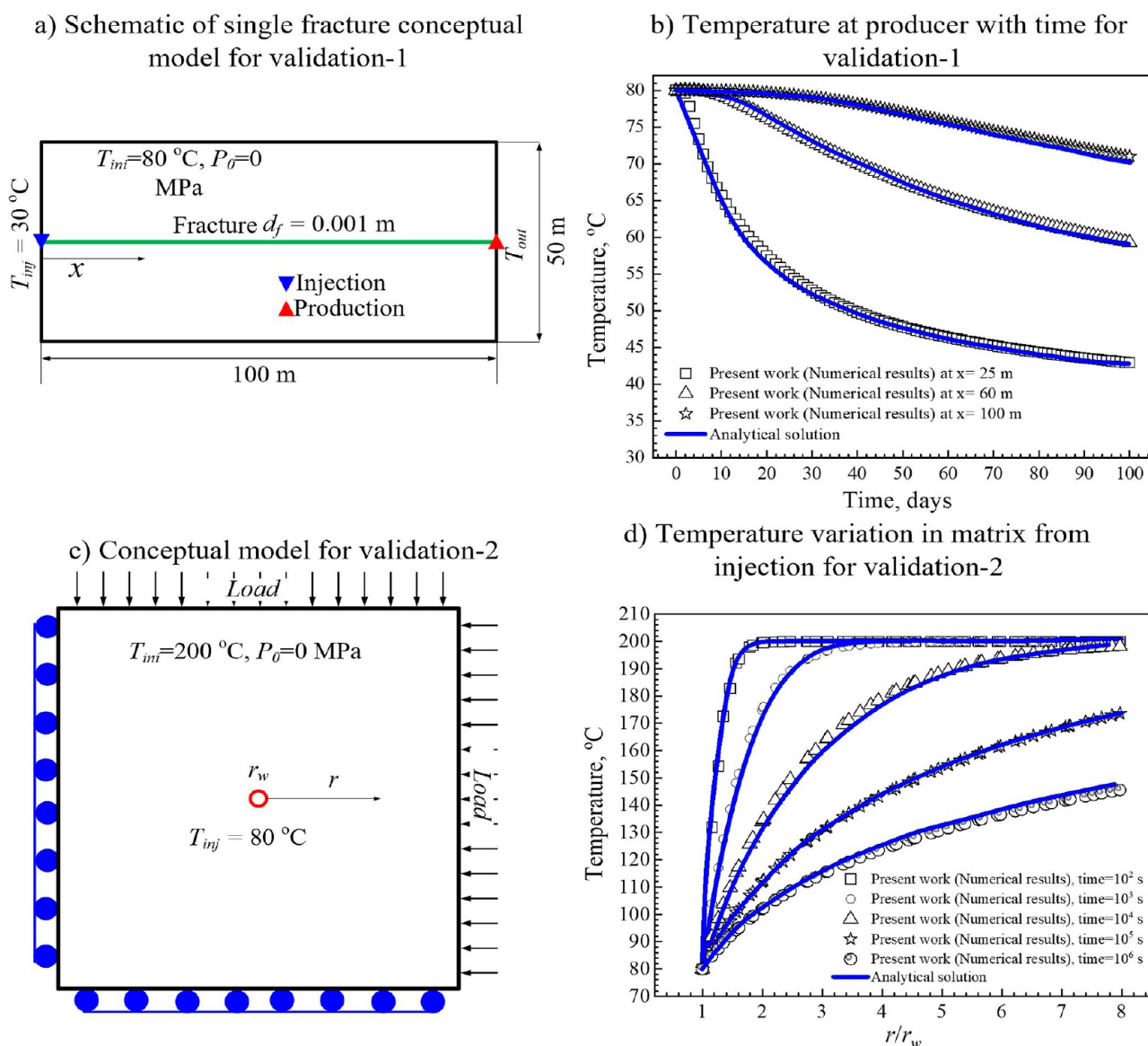


Figure 5. Validation of the developed THM model with the single fracture case and only the rock matrix case.

RESULTS AND DISCUSSION

Validation. The fully coupled THM model is validated with a single fracture scenario and the rock matrix without a fracture. The analytical solution given by Lauwerie⁹³ in eq 49 is used to validate the model developed. Figure 5a,c presents the geometry details of validation-1 and validation-2, respectively. The rock and fluid properties were taken from the works of Ghassemi and Zhang⁸¹ and Han et al.⁹⁴

$$T(x, t) = T_0 + (T_{inj} - T_0) \operatorname{erfc} \left[\frac{\lambda_m x}{\rho_w C_{pw} d_f \sqrt{\frac{\lambda_m}{\rho_m C_{pr}} (u_w t - x)}} \right] U \left(t - \frac{x}{u_w} \right) \quad (49)$$

The results of the developed THM model and their comparison with analytical solutions are presented in Figure 5b,d for validation-1 and validation-2, respectively. A comparison of the results obtained from the developed THM model

with analytical solutions shows a high precision. This confirms that the developed THM model is suitable for predicting thermo-hydromechanical variations in both the rock matrix and fractures. Therefore, the developed model is applied to investigate the variations that occur in fractured geothermal reservoirs.

Temperature Evolution. Figure 6 illustrates the spatial and temporal distribution of temperature in porous media in different arrangements of natural fractures when SCCO₂ is used as a geofluid. In the early stages, heat transfer occurs between the matrix and the geofluid in the hydraulic fracture. Due to the heat conduction between the geofluid and the rock matrix, the temperature of the geofluid increases (Figure 6). During this period, the temperature of the rock matrix in the vicinity of the hydraulic fracture decreases, creating a low temperature region that advances into the rock matrix over time. This reduces the production temperature as a result of the lower extraction of heat compared with the initial stage. It is efficiently identified after five years of production (Figure 6). The geofluid mass and heat exchange are maximized in the injection well locality. The influence of natural fractures on the temperature

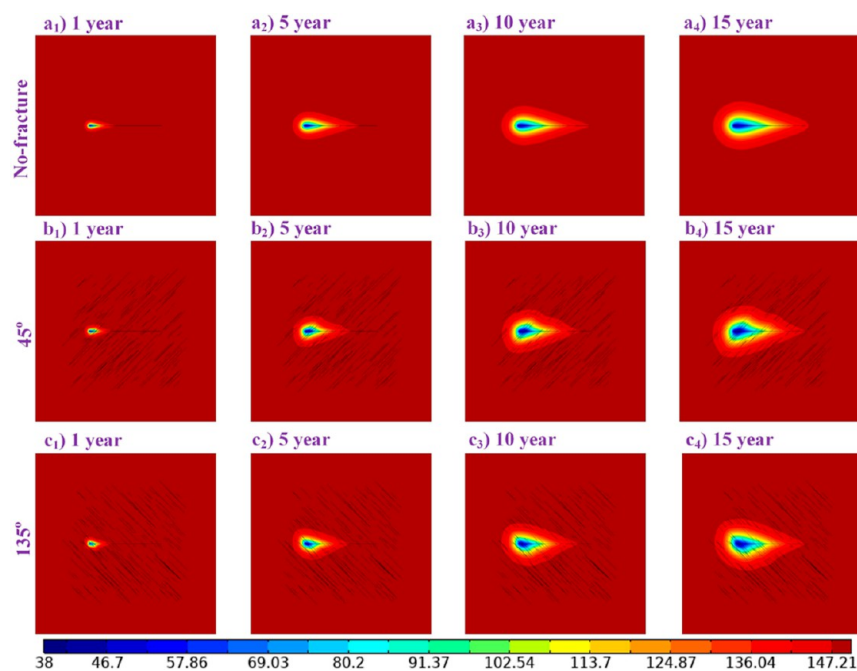


Figure 6. Spatiotemporal variation of temperature in the reservoir at different arrangements of natural fractures while using SCCO_2 as geofluid.

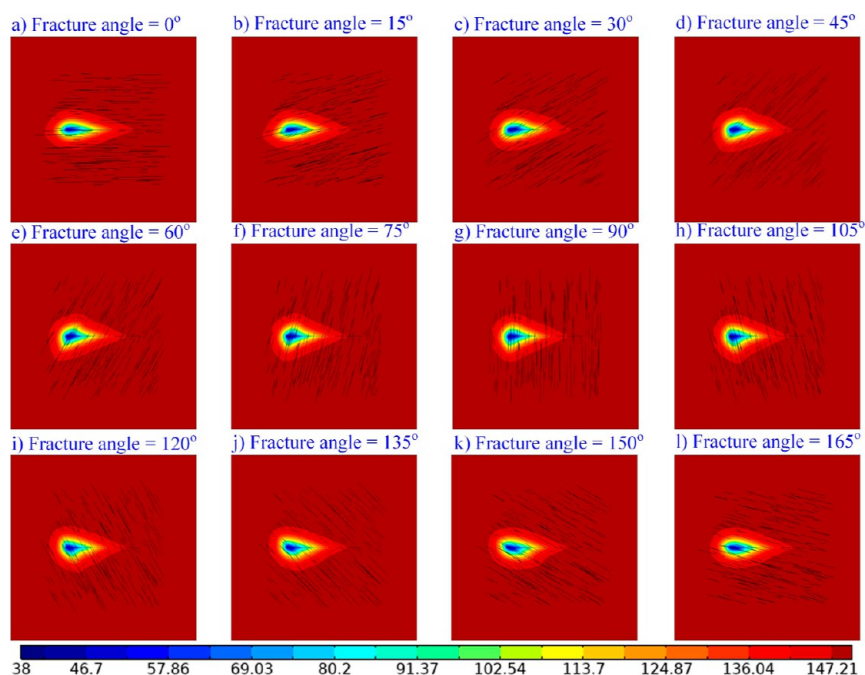


Figure 7. Spatial variation of temperature in the reservoir at different arrangements of natural fractures after 10 years of production.

distribution is investigated and presented in Figures 6 and 7. It is clearly found that the injected fluid moves from the hydraulic fracture to the natural fracture before reaching the production well (Figure 6b₁–b₄, c₁–c₄). It can be seen from the numerical results that the zone adjacent to the hydraulic fracture is highly influenced at the beginning of heat production (Figure 6a₁–a₄) and expands through the natural fracture connected in the reservoir (Figure 6b₁–b₄, c₁–c₄). Figure 7 shows the spatial distribution of the temperature in the reservoir after 10 years of production. The distribution of the low temperature zone depends on the orientation of the natural fractures and the connectivity of the hydraulic fractures. Thus, numerical

investigations clearly identify the influence of natural fractures on the expansion of the low-temperature zone.

Figure 8 represents the impact of the hydraulic fracture aperture and the injection and production (inj/prod) velocity on the temperature of the production well. It is found that an increase in the aperture of the hydraulic fracture reduces the temperature in the production well. This is due to the low residence time before reaching the production well for small aperture scenarios (Figure 8a), which decreases the transfer of heat from the matrix to the geofluid. The temperature in the production well decreases with an increase in inj/prod velocity, as illustrated in Figure 8b. At a higher inj/prod velocity (0.04 m/

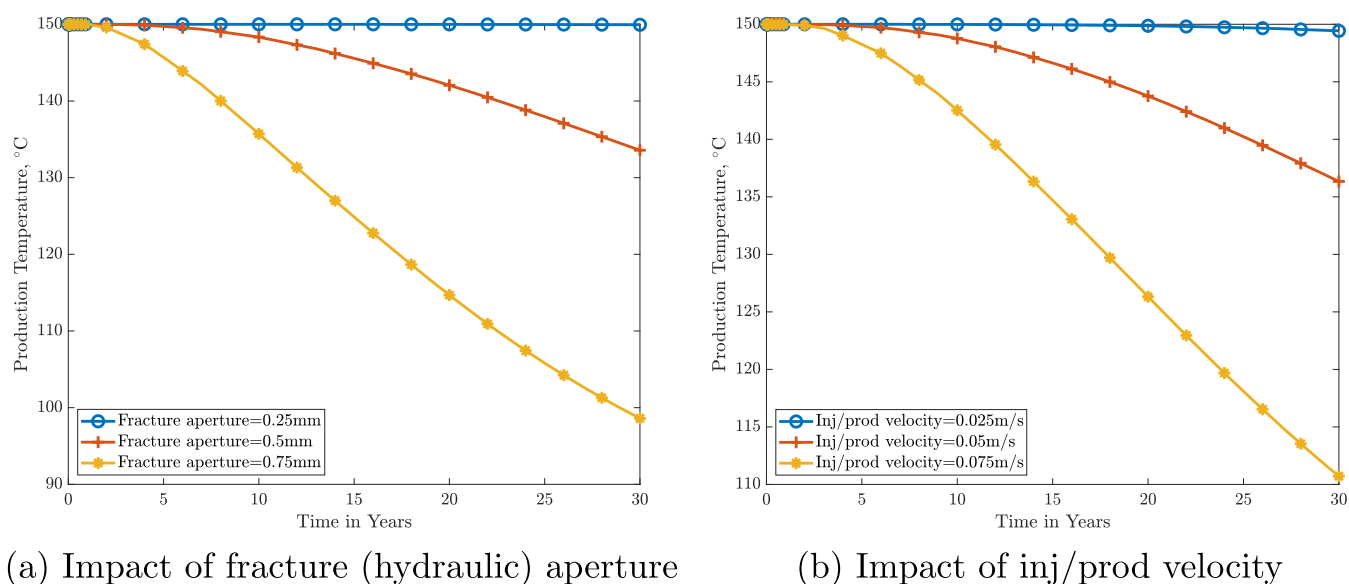


Figure 8. Impact of fracture aperture (fracture angle = 0°, inj/prod velocity = 0.05 m/s) and injection/production velocity (Fracture angle = 15°, fracture aperture = 0.5 mm) on production temperature.

s), the fluid moves faster in the hydraulic fracture, leading to a low residence time. As a result, the fluid has shorter time to transfer heat from the surrounding rock matrix before reaching the production well, which is consistent with our previous work.⁵⁵ Thus, the production temperature is lower compared to the low inj/prod velocity (0.01 to 0.03 m/s).

Figure 9 depicts the influence of the orientation of the fracture on the production temperature under the same operating conditions. It is found that the orientation of natural fractures significantly impacts the production temperature, unlike the hydraulic fracture aperture and inj/prod velocity. Therefore, the aperture of the hydraulic fracture, the inj/prod velocity, and the orientation of the natural fractures influence the temperature at the production well.

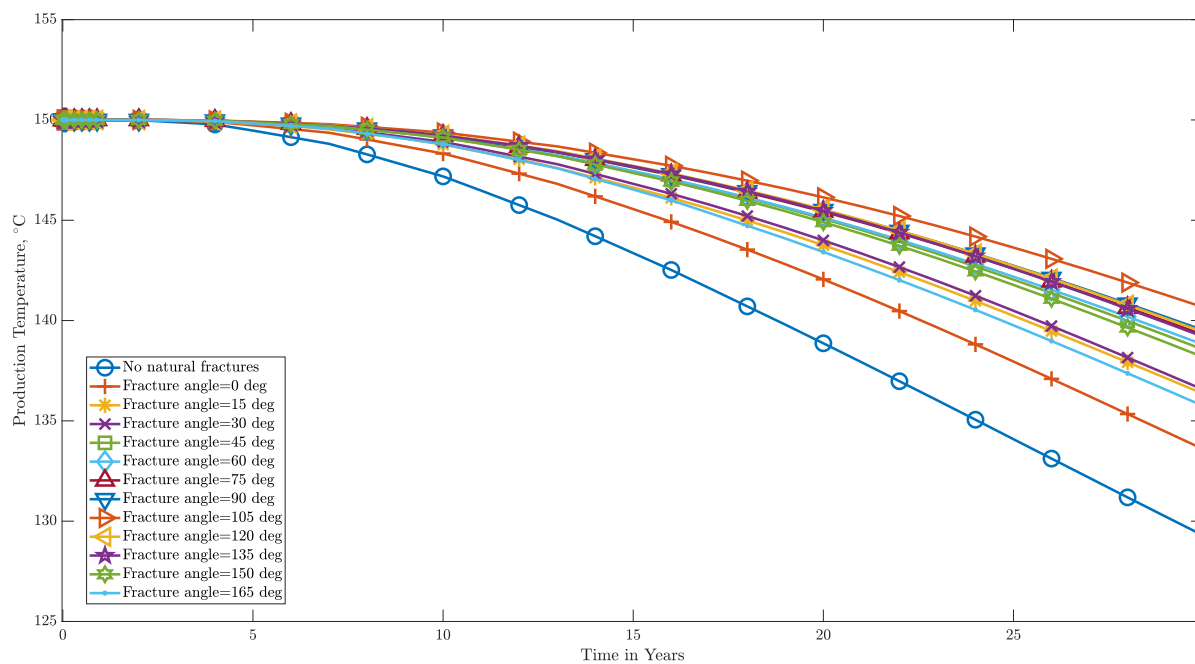
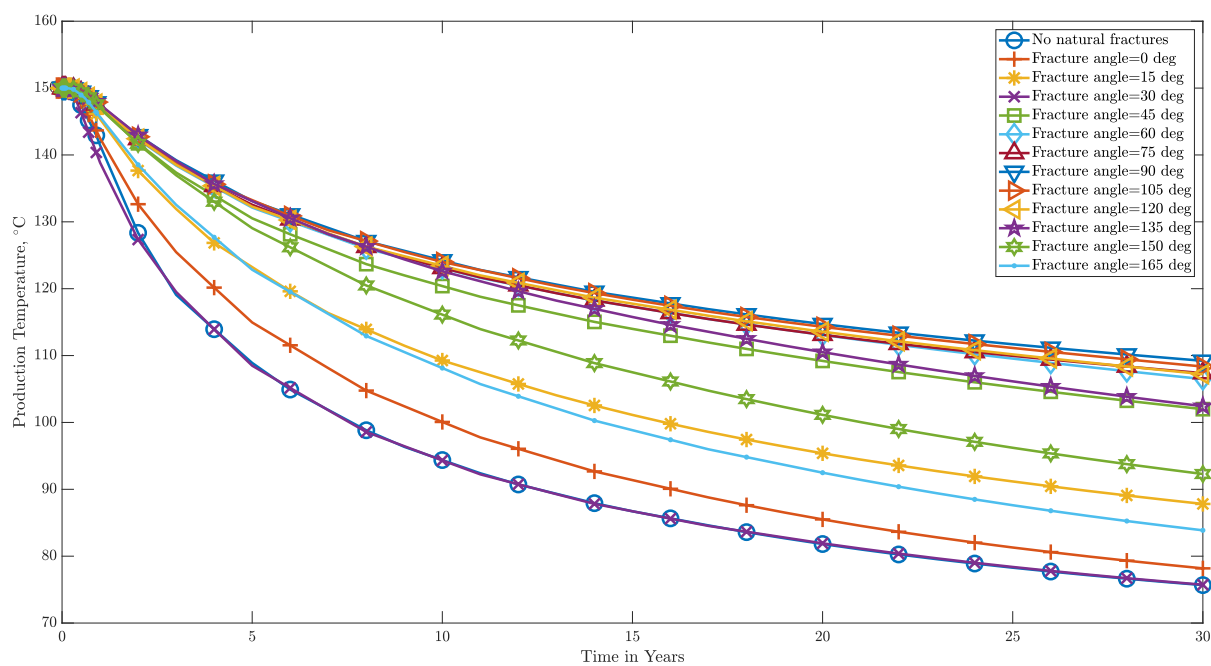
Figure 10 depicts a comparison of SCCO₂ and water as geofluids and illustrates the impact of geofluid type on production temperature and produced heat energy at the same operating conditions. It is found that the production temperature decreases dramatically with the progression of the operational time when using water compared with SCCO₂ (Figure 10a). The angle of the natural fractures also significantly affects the production temperature but does not follow any sequential trend. Similarly, thermal breakthrough is faster when water is used as the geofluid. The net heat energy produced at the bottom hole is depicted in Figure 10b. Net heat energy is determined using eq 50.

$$W_{\text{net}} = (\dot{m}H)_{\text{prod}} - (\dot{m}H)_{\text{inj}} \quad (50)$$

The net heat energy also follows the same trend as the production temperature. Initially, the net heat energy starts at the same point and then decreases as the production temperature drops. This decline is very sharp in the case of water as geofluid. The net heat energy produced using SCCO₂ is higher than that of water as a geofluid. This is due to the higher production temperatures in the SCCO₂ as in geofluid cases. Thus, SCCO₂ provides a better production temperature and net extraction of heat energy compared to water as a geofluid from the same fractured reservoir under similar operating conditions.

Evolution of Strain. The importance of strains generated due to thermal and mechanical variations in the reservoir has been extensively studied. Figure 11 represents the spatial and temporal disparity of thermal and mechanical strains. The volume of rock matrix variation due to the temperature difference is called thermal strain. It is found that the strain generated due to the temperature variation is highly active near the hydraulic fracture and injection well. The maximum thermal strain is identified near the injection well, and the lowest is observed in the production well (Figure 11a,b). The minimum strain generated due to mechanical variation is found in the low temperature zone (Figure 11c,d). Thus, strains generated due to thermal variation are more active in the low-temperature zone, and geomechanical stresses are influential in the rest of the area (i.e., away from the low-temperature zone). The type of geofluid has a significant impact on the region of the reservoir where thermal and mechanical deformation occur (Figure 11). The low temperature region is more prominent when water is used as a geofluid compared to SCCO₂. Due to this, thermal strains are more significant when using water in the low-temperature region compared to SCCO₂. Thus, the type of fluid strongly influences the thermal and mechanical strains.

The spatial variation of the stress in the reservoir is presented in Figure 12. Compressive stresses are observed to dominate the reservoir due to the applied boundary conditions. These stresses change over time in the vicinity of the injection well and along the fracture. It is clearly identified in the present work and is depicted in Figure 12. Due to this, the porosity and permeability in the vicinity of the injection well and along the fracture will enhance and improve the flow and heat transfer. The impact of injection/production rates on the effective stress generated in the rock matrix and fractures is studied and presented in Figure 13. It is found that the effective stress is compact in nature (i.e., negative effective stress) at lower inj/prod velocities (i.e., 0.025). The spatiotemporal evolution of effective stress in the reservoir is presented in Figure 13. It shows that with the compression stress is dominating in the vicinity of hydraulic fracture. With an increase in the velocity, the magnitude of the effective stresses decreases in the vicinity of the hydraulic fracture during the heat extraction operation (Figure 13a–c).

(a) $SCCO_2$ as geofluid

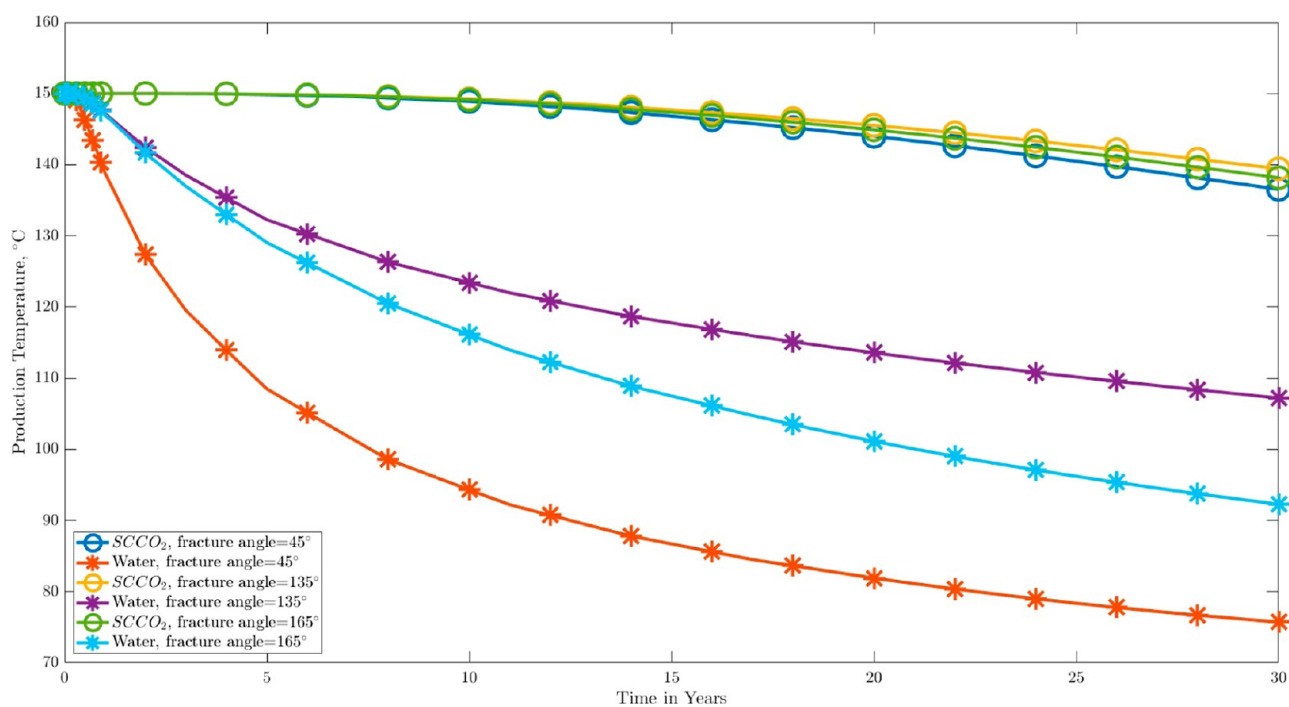
(b) Water as geofluid

Figure 9. Impact of natural fractures angle on production temperature ($^{\circ}\text{C}$) while using $SCCO_2$ and water as geofluids.

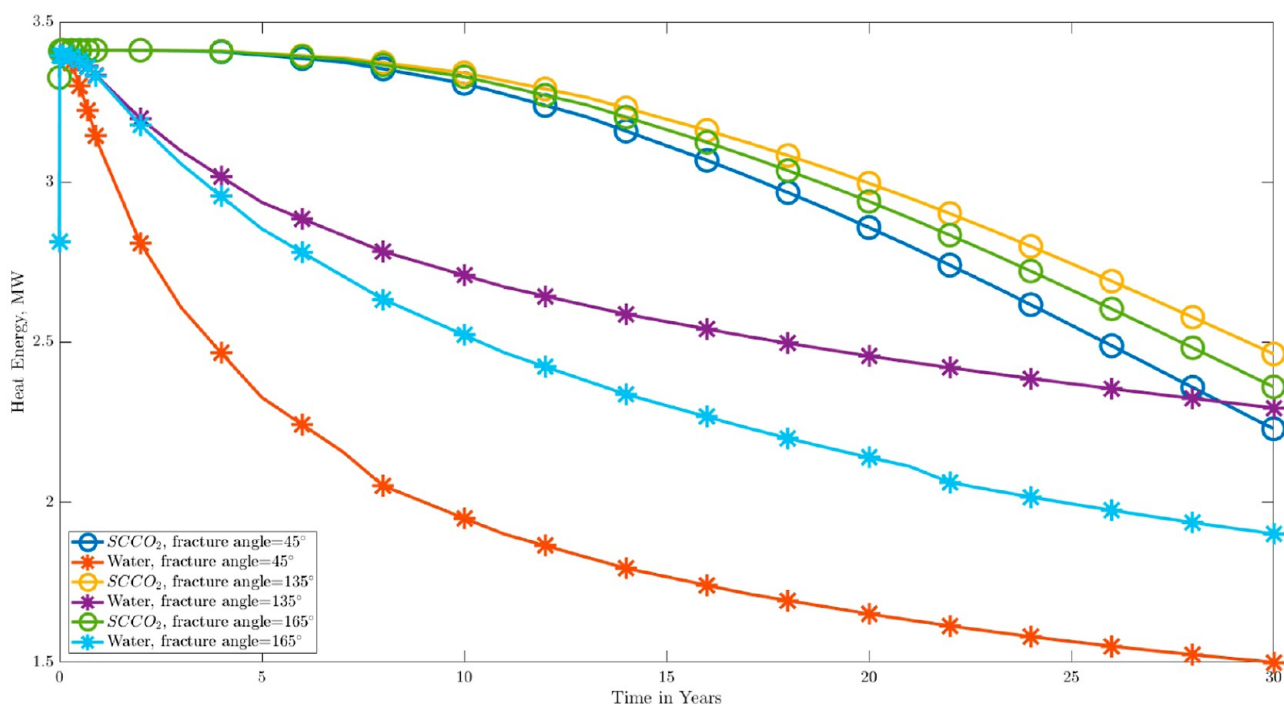
Similarly, effective stress on fractures will influence their permeability, further affecting the heat extraction procedure (Figure 13d–e). The higher magnitude of negative stresses would enhance the permeability of the fracture, which increases the velocity of fluid flow within the fractures. The higher magnitude of stress is found to accumulate in the vicinity of the injection well and progress toward the production well. These

stress accumulations occur in the vicinity of the hydraulic fracture and the natural fracture, which are influenced by the injected fluids (Figure 14).

The impact of maximum and minimum stresses on the heat extraction performance of the fractured geothermal reservoir is also studied. It is found that production decreases with an increase in the applied stress for the same operating conditions.



(a) Production temperature



(b) Net heat energy

Figure 10. Comparison of SCCO₂ and water as geofluids on the production temperature (°C) and heat energy (MW).

An increase in the external loads to the reservoir's boundaries directly influences the effective stress in the rock matrix and fractures. With an increase or decrease in the external load, the fracture permeability is affected, which can directly influence the

flow of cold fluid in the fracture. With an increase in external loads, the permeability of the fractures increases, and the injected fluid reaches much faster compared to lower loads. It is reflected directly in the production temperature. Thus, applying

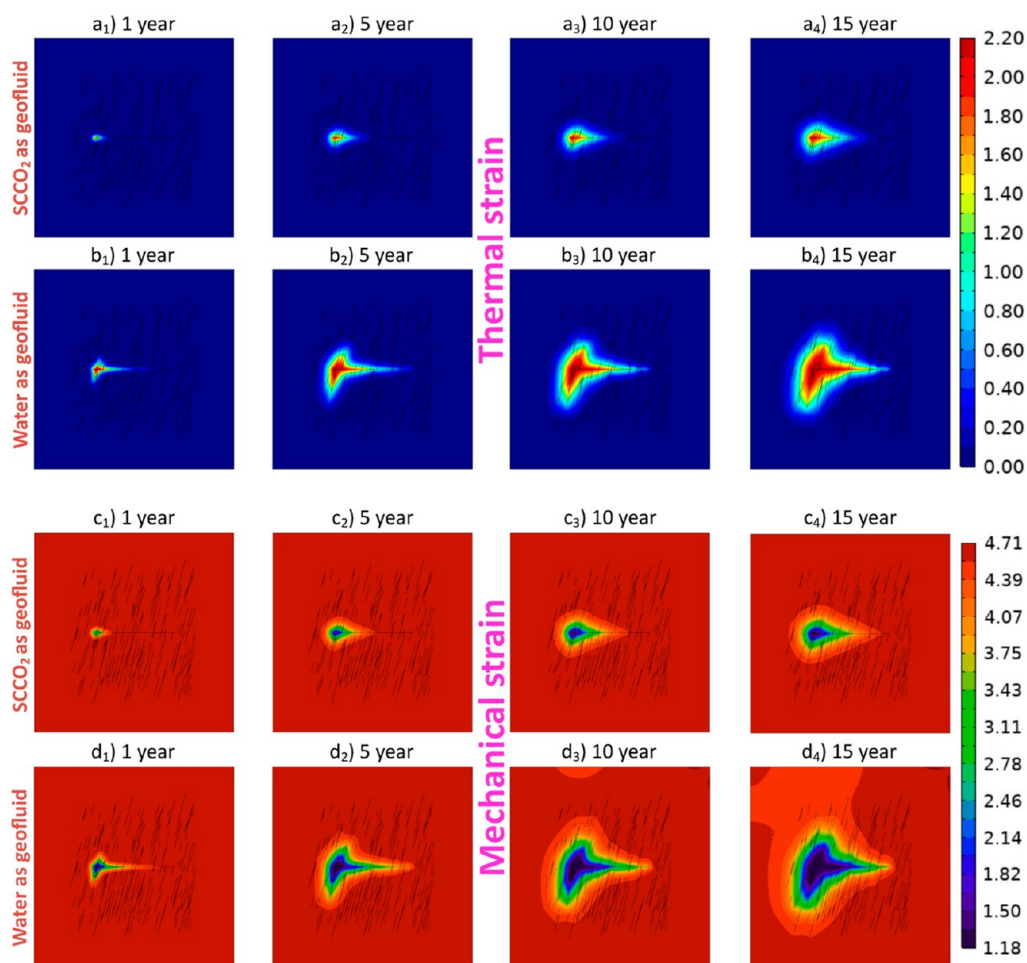


Figure 11. Comparison of SCCO₂ and water as geofluids on thermal and mechanical strains ($\times 10^{-3}$) at a natural fracture orientation of 75°.

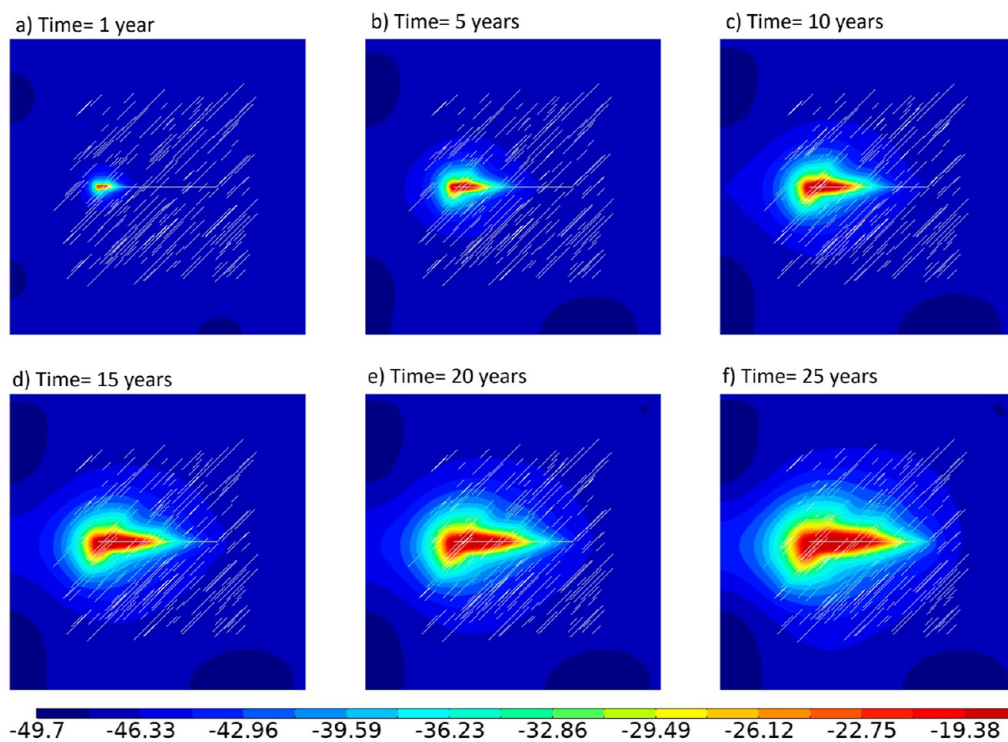


Figure 12. Spatial and temporal variation of stress in the reservoir with a natural fracture orientation of 75°.

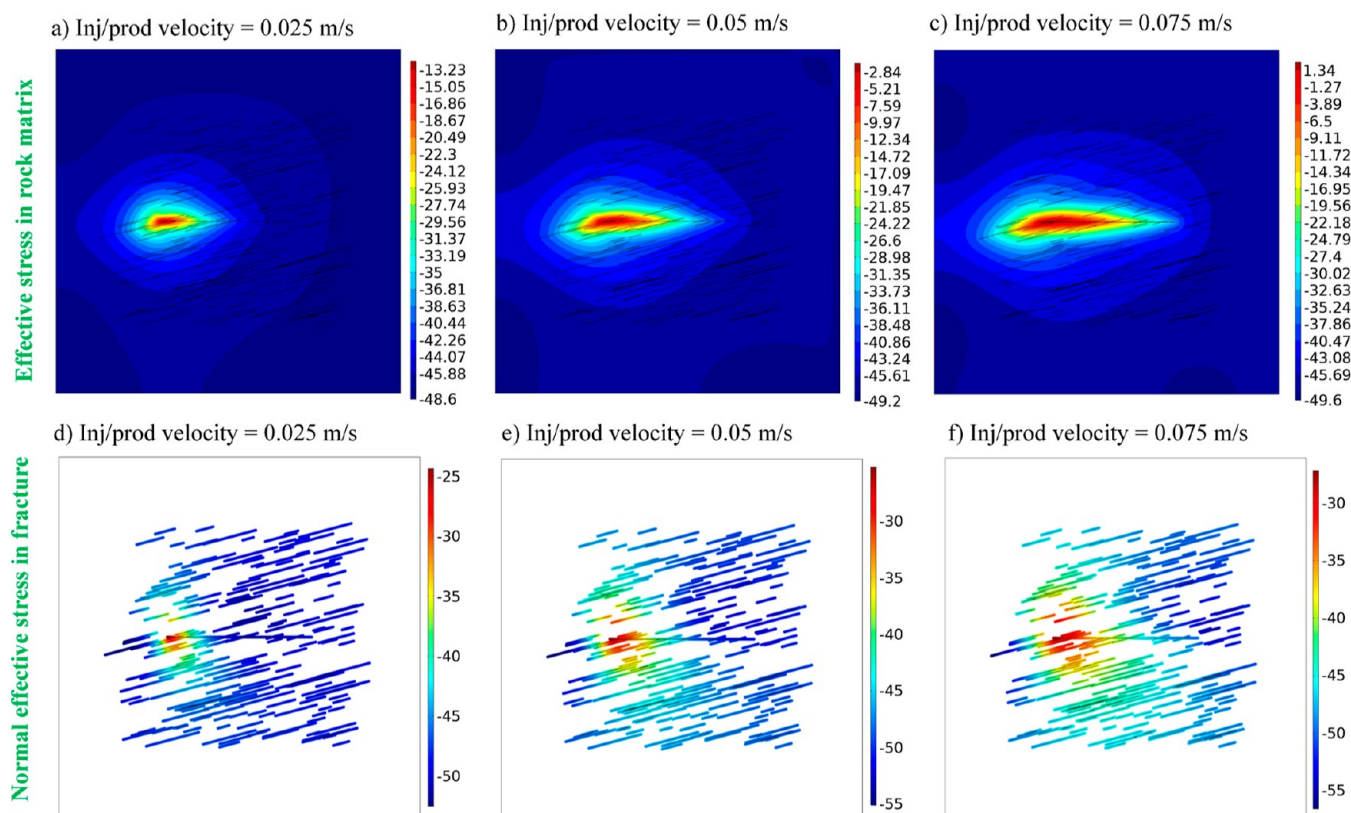


Figure 13. Effective of injection/production velocities on the stress distribution in rock matrix and fractures after 20 years of operation (natural fracture angle = 15°).

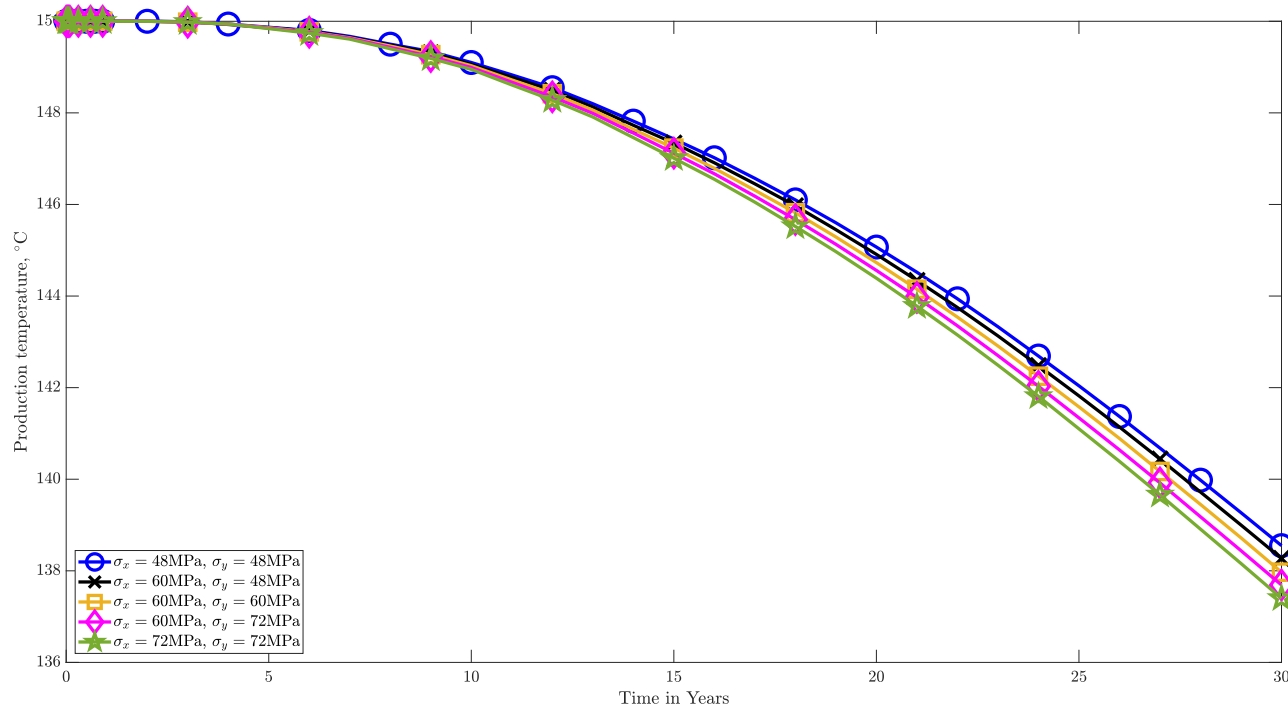


Figure 14. Influence of stresses in the production temperature (natural fracture angle = 45°).

suitable external loads to the geothermal load is essential and improves the thermal/cold front movement and production temperature prediction during the operation.

NN Model for Geothermal Reservoirs. *Neural Networks.* NNs are employed successfully in various fields such as medical,

engineering, economics, mathematics, and more, for identifying patterns, sounds, and speech, and forecasting the stock market, rain, weather, etc. In recent years, the application of NNs in the geoscience and hydrocarbon sectors has gained more popularity, including the prediction of crude oil production, rock properties,

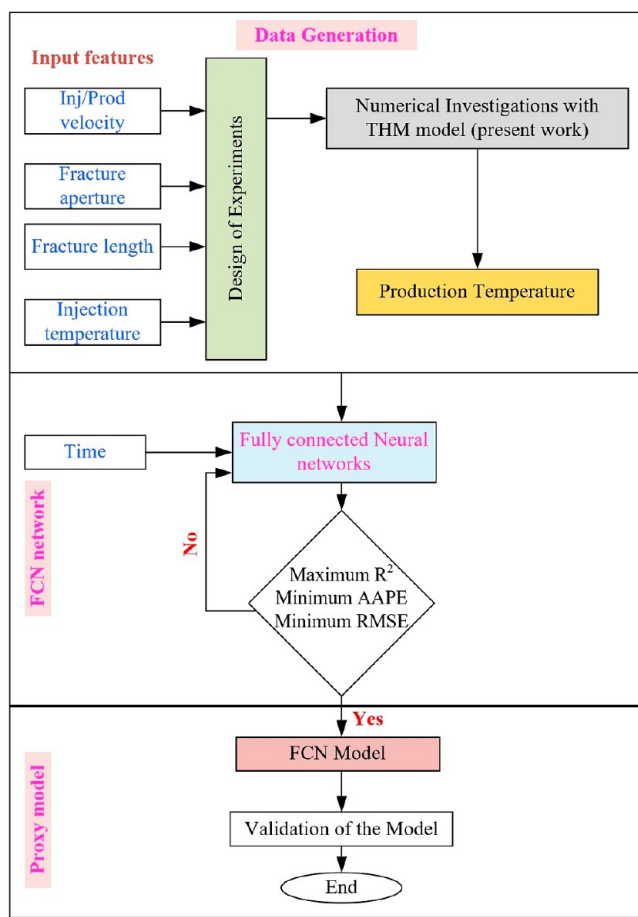


Figure 15. Schematic of the flow scheme from the experimental design to FCN.

Table 3. Influencing Parameter and Its Ranges with Units

name of factor	unit	lower limit	higher limit
injection temperature	°C	35	45
fluid injection/production velocity	m/s	0.025	0.05
fracture aperture	Mm	2	6
fracture length	m	200	300

and the recognition of seismic patterns.^{1,46–50,55–58,95} NNs are nontraditional tactics in which they are accomplished to study systems of solutions rather than being programmed to model a specific problem normally. They are widely recognized as a technology that provides an alternative way to address complex problems and an alternative to complex rules. NNs can learn the key information from the multilayered information provided in the form of data. NNs contain an input layer (IL), an output layer (OL), and these are connected with a series of hidden layers (HL). Each HL has a number of neurons that receive information from the previous neuron for processing.

Mathematical Model Based on FCN to Predict Production Temperature. In this work, a time series model is being developed using the FCN model. The FCN model is utilized to develop a mathematical model for predicting the production temperature by using the influencing parameters. The flow structure from the input features to the development of the FCN model is presented in Figure 15. The first section involves the data generated using the design of experiments. The temporal data of the production temperature were collected from the

Table 4. Qualitative Numerical Experimentation's for Deep NNs

Sl. no	hydraulic fracture length, m	hydraulic fracture aperture, mm	injection temperature, °C	injection/production velocity, m/s
1	250	4	40	0.0375
2	200	2	45	0.025
3	300	6	45	0.025
4	200	6	45	0.05
5	300	2	35	0.05
6	200	4	40	0.0375
7	250	4	45	0.0375
8	200	6	45	0.025
9	300	4	40	0.0375
10	250	4	40	0.0375
11	300	6	35	0.025
12	200	2	35	0.025
13	250	4	40	0.025
14	250	4	40	0.0375
15	250	6	40	0.0375
16	300	6	35	0.05
17	200	6	35	0.05
18	250	4	40	0.05
19	250	4	40	0.0375
20	250	2	40	0.0375
21	300	2	45	0.05
22	250	4	40	0.0375
23	200	2	35	0.025
24	300	6	45	0.05
25	200	2	45	0.05
26	200	6	35	0.025
27	250	4	40	0.0375
28	250	4	35	0.0375
29	300	2	35	0.025
30	300	2	45	0.025

production well. In the second section, a FCN is developed with a single hidden layer over time as an additional input feature. The data collected from the first section are used to develop a proxy model (i.e., Section Geological Model for the Heat Extraction from Geothermal Reservoir). The full structure of the FCN model is provided as follows.

Computational Geometry. A new geometry of computation is designed for the hybrid FCN model and is presented in Figure 2b. A complex natural fracture network is created using power law and Fisher distributions, as presented in Section. The aperture of the natural fracture ranges from 0.1 to 5 mm, the length of the natural fractures varies from 1 to 50 m, and the orientations vary from 0° to 165°. The same initial and boundary conditions are imposed, except for injection temperature, fracture aperture, fracture length, and injection/production velocity, which are considered as influencing parameters in the present work.

Sampling. The training data are generated by utilizing the design of the experimentation technique. RSM is applied for qualitative numerical experimentation. A total of four influencing parameters are identified, and the RSM is designed for 30 numerical experiments (Figure 15). Table 3 provides the minimum and maximum ranges of the influencing parameters, and Table 4 illustrates the qualitative experiments designed to carry out the numerical simulations. These numerical experiments will provide adequate training and validated data sets for

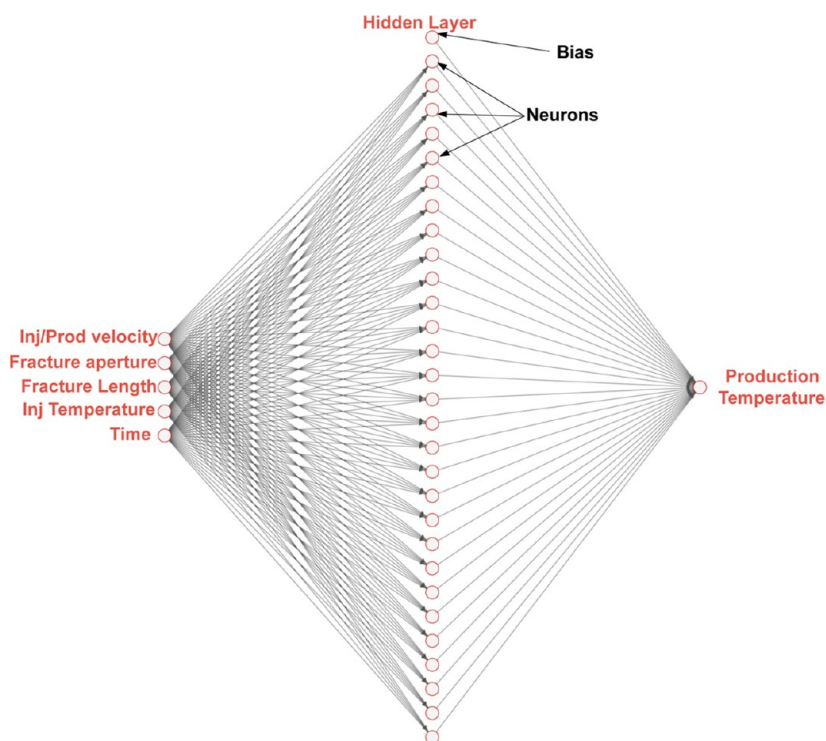


Figure 16. Schematic of the FCN model used to predict the production temperature.

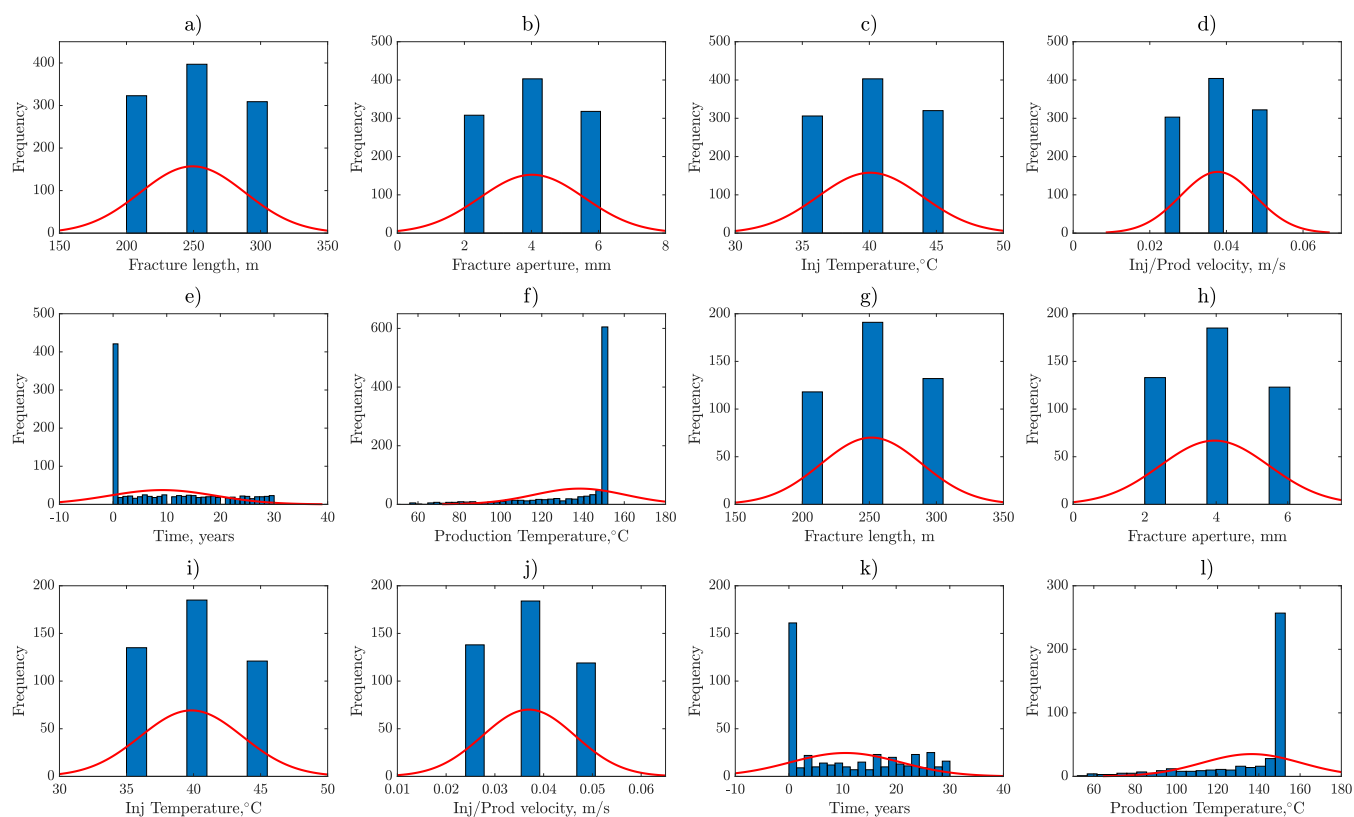


Figure 17. Histogram of training (a–f) and testing (g–l).

the FCN model to evaluate the influence of input parameters on the temperature in the production well.

Input Layer. The IL includes five nodes, which include the injection temperature, fracture aperture, fracture length, inj/prod velocity, and time.

Output layer. The OL consists of one output node, and it is the production temperature, which is obtained from the numerical simulations.

Hidden Layer. The number of input nodes in the input layers varies and depends on the problem statement. It is not possible

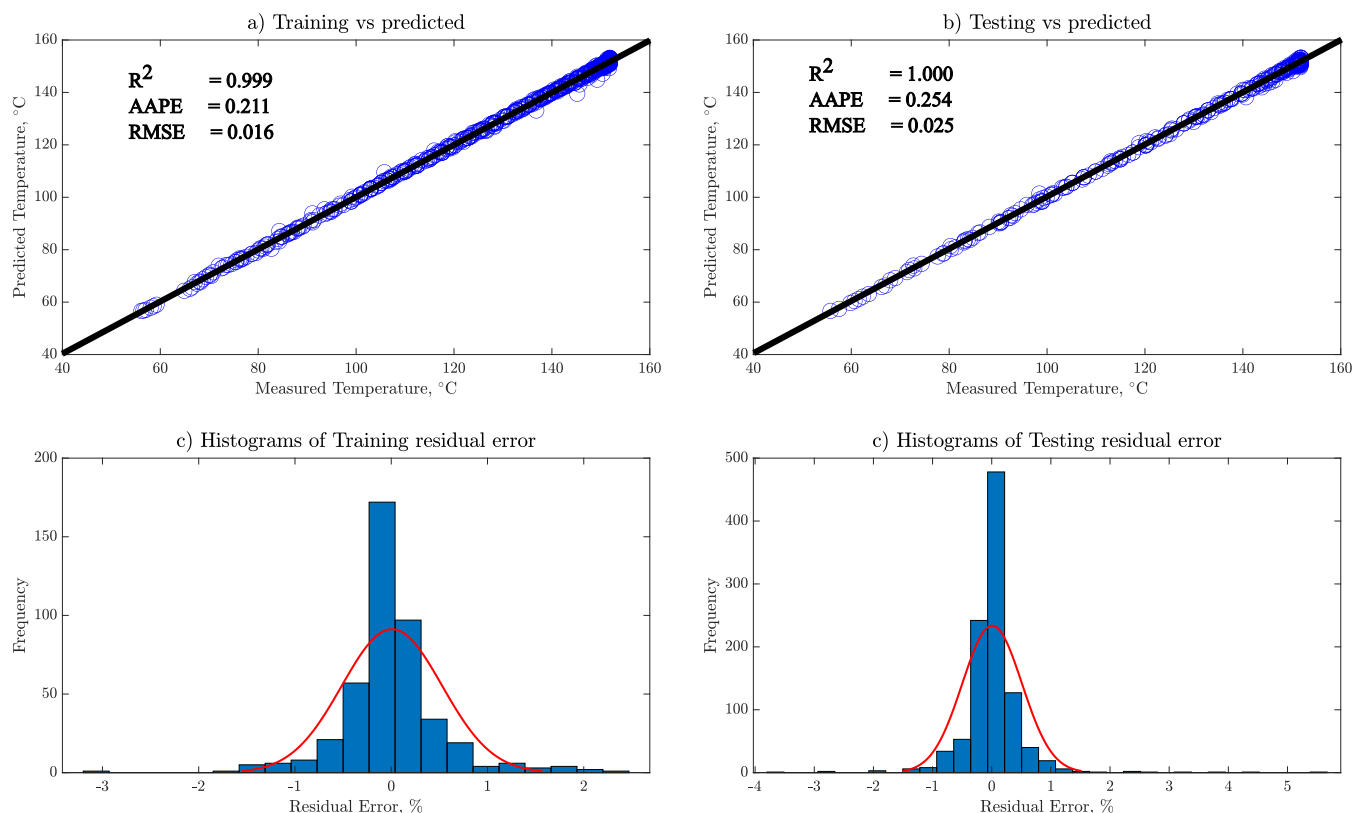


Figure 18. Production temperature of numerical simulations vs DNN model predicted with residual error histograms.

to use the same architecture for all problem statements. For the optimal architecture of the FCN and better accuracy, in the present work, we utilize 30 neurons and bias.

Objective/Loss Functions. In this work, the FCN model is used to estimate the temporal changes that occur in the temperature in the production well. There are various error calculation tools available in the design of the DNN models. In this work, the average absolute percentage of error, the mean square error, and the coefficient of determination (R^2) are applied as error estimation (loss) functions. Equations from eqs 51–53 represent the loss functions used in the design of DNN models.

$$\text{AAPE} = \frac{100}{n_{TR}} \sum_{i=1}^{n_{TR}} (T_{p-DNN} - T_{p-data}) \quad (51)$$

$$\text{RMSE} = \sqrt{\frac{\sum_{i=1}^{n_{TR}} (T_{p-DNN} - T_{p-data})^2}{n_{TR}}} \quad (52)$$

$$R^2 = 1 - \frac{\sum_{i=1}^{n_{TR}} (T_{p-data} - T_{p-DNN})^2}{\sum_{i=1}^{n_{TR}} (T_{p-DNN} - T_{avg,p-data})^2} \quad (53)$$

Mathematical Equation to Estimate Production Temperature. The structure of the FCN is presented in Figure 16. The distributions of the input and output parameters used in training and testing are presented in Figure 17. Figure 18a depicts the cross plots of the training and testing data, which show greater precision in the prediction of the production temperature. The residual errors accumulated within -2 to 2 for training and testing data (Figure 18). A mathematical model is developed using the above FCN model with influencing parameters. The

hidden layer neuron uses its weight w_1 and bias b_1 , and the mathematical expression is presented in eq 54.

$$\sigma_{\text{tf},L}(\sum_{j=1}^{N_p} w_{1,j} x_j + b_1) \quad (54)$$

The output of the whole network will be expressed in eq 55

$$\mu_p(\varphi) = \sigma_{\text{tf},0}[\sum_{i=1}^{N_h} w_{2,i} \sigma_{\text{tf},L}(\sum_{j=1}^{N_p} w_{1,j} x_j + b_1) + b_2] \quad (55)$$

Here, $\sigma_{\text{tf},L}(x) = \left(\frac{2}{1 + e^{-2x}} - 1\right)$, and $\sigma_{\text{tf},0}(x) = x$. The proposed equation of FCN of the production temperature can be written more specifically as in eq 56

$$T_{\text{prod}} = 103.75 - 48.05 T_{\text{prod},n} \quad (56)$$

The equation for the $T_{\text{prod},n}$ is given in eq 57

$$T_{\text{prod},n} = \sigma_{\text{tf},0}[\sum_{i=1}^{N_h} w_{2,i} \sigma_{\text{tf},L}(X_1) + b_2] \quad (57)$$

$$X_1 = w_{1,i,1} L_{f,n} + w_{1,i,2} d_{\text{afrc},n} + w_{1,i,3} T_{\text{inj},n} + w_{1,i,4} v_{\text{inj}/\text{prod},n} + w_{1,i,5} t_n + b_{1,i} \quad (58)$$

The expressions for the normalized terms such as $L_{f,n}$, $d_{\text{afrc},n}$, $T_{\text{inj},n}$, $v_{\text{inj}/\text{prod},n}$ and t_n were presented from eqs 59–63.

$$L_{f,n} = 5 - 0.02 L_f \quad (59)$$

$$d_{\text{afrc},n} = 2 - 0.5 d_{\text{afrc}} \quad (60)$$

$$T_{\text{inj},n} = 8 - 0.2 T_{\text{inj}} \quad (61)$$

$$v_{\text{inj}/\text{prod},n} = 3 - 80 v_{\text{inj}/\text{prod}} \quad (62)$$

$$t_n = 1 - 0.066 t \quad (63)$$

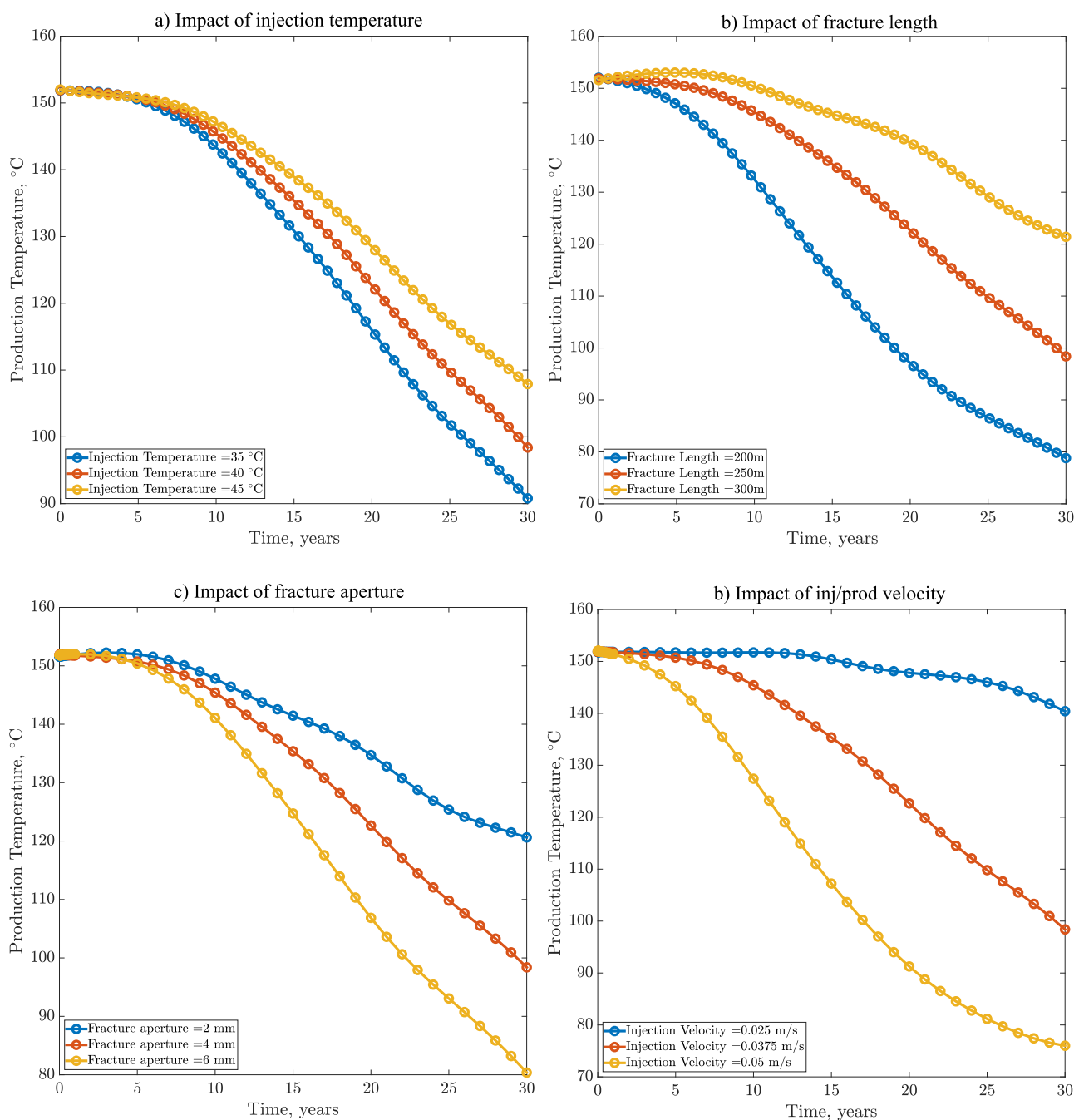


Figure 19. Impact of influencing parameters on the production temperature (i.e., results from eq 57).

Here, L_f in m, d_{afc} in mm, T_{inj} in °C, $v_{\text{inj/prod}}$ in m/s, and t is in years. The mathematical model developed with FCN shows greater precision with the simulated results, and the coefficients are listed in Table 5. Figure 19 shows the impact of influencing the production temperature, and a similar impact is observed from the simulation results (i.e., Figure 8). The accuracy of the developed mathematical model is also checked with ten random scenarios and compared with the simulated results. In Figure 20, it is found that the mathematical model developed shows results similar to the simulated results. Therefore, the mathematical model developed can be utilized to predict the temporal evolution of the production temperature of a fractured geothermal reservoir within the desired limits.

CONCLUSIONS

In the present research work, we use the fully coupled THM model to examine the behavior of a geothermal reservoir. In the present work, we consider the dynamic behavior of fluid, rock, and fracture properties and examine the influence of natural fractures and their orientation. We utilized COMSOL Multiphysics software for numerical experimentation using the THM model. The effect of SCCO₂ as a geofluid for heat extraction has also been extensively studied and compared to that of water as a geofluid.

The temperature in the production well and the low temperature zone in the rock matrix are impacted by the injection/production velocity, the hydraulic fracture aperture, and the orientation of the natural fracture. Production

Table 5. Weights and Biases of the Optimized NN Model

neurons	weights between input and hidden layer (w_1)					weights between hidden and output layer (w_2)	bias between input and hidden layer (b_1)	bias between hidden and output layer (b_2)
	$L_{t,n}$	$d_{\text{afc},n}$	$T_{\text{inj},n}$	$v_{\text{inj}/\text{prod},n}$	t_n			
1	0.530	-0.588	0.162	-2.465	-1.944	0.438	2.754	
2	-0.846	-0.965	-0.278	1.005	-0.783	-0.319	3.745	
3	1.316	1.576	1.926	-0.222	-2.134	0.052	0.785	
4	-0.892	3.643	-1.015	-2.038	0.471	0.067	2.110	
5	-0.003	1.164	-3.465	-2.910	-0.120	-0.075	2.948	
6	-1.988	3.694	0.281	0.187	1.075	-0.039	1.139	
7	-0.113	-1.434	-2.841	1.038	-0.003	-0.068	-1.059	
8	1.363	-1.940	3.105	1.271	2.411	0.068	-1.272	
9	-0.047	-0.007	0.042	0.933	2.952	-0.178	0.766	
10	-1.546	-3.237	-0.747	-0.380	-0.062	-0.213	-0.978	
11	-2.173	0.386	-1.199	1.140	-1.371	-0.069	1.791	
12	1.325	1.914	-1.833	0.328	-0.210	-0.211	-1.293	
13	1.191	1.767	2.874	-0.609	-1.482	-0.164	-0.574	
14	0.802	-3.961	-0.387	0.801	2.324	0.141	-4.276	
15	0.430	-0.183	0.043	-1.651	-2.571	0.311	0.895	
16	-3.720	1.981	1.765	1.129	-1.357	0.111	-0.126	
17	0.243	-1.162	-2.589	0.313	-2.034	0.042	-0.357	
18	1.224	-0.374	-1.156	3.432	-1.421	0.151	0.131	
19	2.476	1.300	-0.107	-3.223	1.036	0.130	0.168	
20	-0.636	-2.689	-0.092	1.677	0.377	-0.241	0.169	
21	-2.487	-3.579	1.644	-0.786	2.596	0.056	-0.291	
22	2.821	2.612	-2.356	-2.287	2.642	0.056	0.357	
23	-2.151	-1.937	-0.682	1.946	-0.090	0.345	-1.162	
24	1.415	4.384	0.284	-1.062	-2.066	-0.047	1.068	
25	-0.662	-0.183	2.816	-0.777	4.132	0.016	-1.602	
26	3.671	-1.015	0.804	-3.300	-1.453	0.111	1.223	
27	4.935	0.070	-1.298	-1.427	-2.790	0.105	3.398	
28	1.906	1.307	2.208	-2.510	-0.495	0.008	3.373	
29	0.163	2.684	-2.063	1.999	-0.598	-0.185	3.304	
30	-1.780	1.102	3.987	-0.532	-0.456	-0.186	3.416	-30×0.745

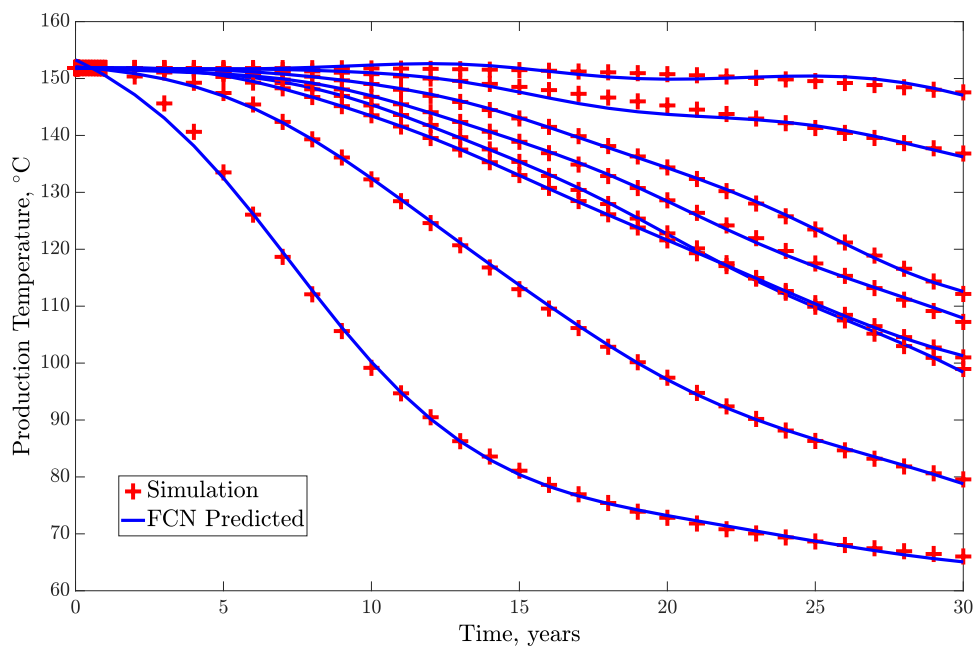


Figure 20. Comparison of simulated results with the equation (i.e., eq 57) developed from the FCN.

temperature decreases with increasing time, injection/production velocity, and hydraulic fracture aperture. A comparison between the water-EGS and SCCO₂-EGS systems is performed

at the production temperature, and the SCCO₂-EGS system has been found to provide promising results compared to those of the water-EGS system. The strain generated due to thermal

drawdown is active in the low-temperature zone, and the strain generated due to mechanical loads is substantial in the rest of the area. Injection/production velocities influence effective stress in both the rock matrix and natural fractures. External load significantly influences the production temperature. The interaction between natural fractures and hydraulic fracture, and the type of geofluid influence the production temperature, thermal strain, mechanical strains, and effective stress in rock/fractures in the geothermal reservoir.

An FCN model is used to forecast the temporal temperature in the production as well as a function of injection temperature, inj/prod velocity, HF aperture, and HF length. RSM is utilized to design numerical experiments without temporal constituents. A mathematical equation is developed to predict the temporal variation of temperature in the production well to a desired level using FCN. Therefore, the numerical simulations developed with the FCN model can be a useful tool to investigate the temporal evolution of the production temperature with higher accuracy.

■ ASSOCIATED CONTENT

Data Availability Statement

The data underlying this study are not publicly available due to copyright issues. Data are available from the corresponding author upon reasonable request.

■ AUTHOR INFORMATION

Corresponding Authors

Zeeshan Tariq – Physical Science and Engineering (PSE) Division, King Abdullah University of Science and Technology (KAUST), Thuwal 23955-6900, Saudi Arabia; orcid.org/0000-0001-5456-7115; Email: zeeshan.tariq@kaust.edu.sa

Bicheng Yan – Physical Science and Engineering (PSE) Division, King Abdullah University of Science and Technology (KAUST), Thuwal 23955-6900, Saudi Arabia; orcid.org/0000-0002-3356-7594; Email: bicheng.yan@kaust.edu.sa

Shuyu Sun – Physical Science and Engineering (PSE) Division, King Abdullah University of Science and Technology (KAUST), Thuwal 23955-6900, Saudi Arabia; orcid.org/0000-0002-3078-864X; Email: shuyu.sun@kaust.edu.sa

Authors

Manojkumar Gudala – Physical Science and Engineering (PSE) Division, King Abdullah University of Science and Technology (KAUST), Thuwal 23955-6900, Saudi Arabia

Suresh Kumar Govindarajan – Reservoir Simulation Laboratory, Petroleum Engineering Programm, Department of Ocean Engineering, Indian Institute of Technology Madras, Chennai 600036, India; orcid.org/0000-0003-3833-5482

Complete contact information is available at:

<https://pubs.acs.org/10.1021/acsomega.3c07215>

Author Contributions

Manojkumar Gudala: conceptualization, methodology, software, validation, formal analysis, writing—original draft, writing—review and editing, and investigations. **Zeeshan Tariq:** Study conceptualization, computational analysis, and manuscript revision. **Bicheng Yan:** software, formal analysis, resources, writing—review and editing, and funding acquisition. **Shuyu Sun:** funding support, study conceptualization, methodology development, and manuscript revision. **Suresh Kumar Govindarajan:** study conceptualization, computational analysis, and manuscript revision.

Notes

The authors declare no competing financial interest.

■ ACKNOWLEDGMENTS

M.G., Z.T., and B.Y. thanks for the Research Funding from King Abdullah University of Science and Technology (KAUST), Saudi Arabia, through the grants BAS/1/1423-01-01 and FCC/1/4491-22-01; M.G. and S.S. thanks for the Research Funding from King Abdullah University of Science and Technology (KAUST), Saudi Arabia, through the grants BAS/1/1351-01-01 and URF/1/4074-01-01; M.G. and S.K.G. gratefully acknowledge financial support from the Indian Institute of Technology—Madras.

■ NOMENCLATURE

Special symbols

$d_{\text{afrc},n}$	normalized fracture aperture
$L_{f,n}$	normalized fracture length
N_p	number of neurons
t_n	normalized time
$T_{\text{inj},n}$	normalized injection temperature
$v_{\text{inj/prod},n}$	normalized injection/production velocity
$w_{1,j}$	weights in hidden layer
x_j	parameters
α_b	Biot–Wills coefficient
α_T	coefficient of thermal expansion
$\Delta\varepsilon_T$	thermal strain
$\Delta\varepsilon_{\text{vol}}$	change in volumetric strain
ΔT	change in temperature
$\frac{d\varepsilon_{\text{vol}}}{dt}$	rate of change in volumetric strain of the porous matrix
$\kappa_{\text{frc}0}$	initial fracture permeability
κ_{frc}	fracture permeability
κ_{mat}	rock permeability
λ_{eff}	effective thermal conductivity
λ_{fl}	thermal conductivity of fluid
λ_{mat}	thermal conductivity of matrix
μ_{fl}	viscosity of the fluid
∇_{T_n}	gradient is measured on the tangential plane of fracture
ν_{frc}	Poisson's ratio of fracture
ϕ_{mat}	porosity of matrix
ϕ_{ini}	initial porosity of matrix
ρ_{fl}	density of fluid
ρ_{mat}	rock density
σ_n	normal stress acting on fracture
σ^*	normalizing constant (and it is considered as the initial reservoir pressure)
a_1	constant
b_1	constant
C_n	coefficient and it is a function of initial porosity of formation and is equal to $5/\phi_i$
$C_{p^{\text{fl}}}$	specific heat capacity of fluid
$C_{p^{\text{mat}}}$	specific heat capacity of matrix
d	fitting parameter (constant and equal to 1)
d_A	damping constant per unit area
d_{afrc}	fracture aperture
E_i	initial elastic modulus
E_{frc}	elastic modulus of fracture
K_A	spring constant
K_d	drained bulk modulus
k_n	stiffness in the normal direction

k_s	shear stiffness
K_{fl}	fluid bulk modulus
M	Biot's modulus
p	pressure
p_{frc}	Pressure in fracture
q_m	source/sink term which couple both matrix and fracture with mechanics
Q_{fracT}	source/sink terms fracture
q_{frc}	flow rate in fractures
Q_{matT}	source term of matrix
$\sigma_{a_{fr,L}}$	activation function
T	temperature
t	time
$T_{avg,p-data}$	mean production temperature of the given data
T_{p-data}	production temperature of the from the training data
T_{p-DNN}	production temperature predicted from the DNN model
u_0	initial displacement of fracture
u_d	displacement in downside of fracture
u_u	displacement in upside of fracture
u_{dlm}	Darcy's velocity
u_{frc}	Darcy's velocity in fracture

REFERENCES

- Zhou, L.; Zhang, Y.; Hu, Z.; Yu, Z.; Luo, Y.; Lei, Y.; Lei, H.; Lei, Z.; Ma, Y. Analysis of influencing factors of the production performance of an enhanced geothermal system (EGS) with numerical simulation and artificial neural network (ANN). *Energy Build.* **2019**, *200*, 31–46.
- Hofmann, H.; Babadagli, T.; Yoon, J. S.; Blöcher, G.; Zimmermann, G. A hybrid discrete/finite element modeling study of complex hydraulic fracture development for enhanced geothermal systems (EGS) in granitic basements. *Geothermics* **2016**, *64*, 362–381.
- Brown, D. W. A hot dry rock geothermal energy concept utilizing supercritical CO₂ instead of water. *Proceedings of the Twenty-Fifth Workshop on Geothermal Reservoir Engineering*; Stanford University, 2000; pp 233–238.
- Biagi, J.; Agarwal, R.; Zhang, Z. Simulation and optimization of enhanced geothermal systems using CO₂ as a working fluid. *Energy* **2015**, *86*, 627–637.
- Zhang, F.-Z.; Xu, R.-N.; Jiang, P.-X. Thermodynamic analysis of enhanced geothermal systems using impure CO₂ as the geofluid. *Appl. Therm. Eng.* **2016**, *99*, 1277–1285.
- Pan, C.; Chávez, O.; Romero, C. E.; Levy, E. K.; Aguilar Corona, A.; Rubio-Maya, C. Heat mining assessment for geothermal reservoirs in Mexico using supercritical CO₂ injection. *Energy* **2016**, *102*, 148–160.
- Zhang, L.; Li, X.; Zhang, Y.; Cui, G.; Tan, C.; Ren, S. CO₂ injection for geothermal development associated with EGR and geological storage in depleted high-temperature gas reservoirs. *Energy* **2017**, *123*, 139–148.
- Pan, L.; Freifeld, B.; Doughty, C.; Zakem, S.; Sheu, M.; Cutright, B.; Terrall, T. Fully coupled wellbore-reservoir modeling of geothermal heat extraction using CO₂ as the working fluid. *Geothermics* **2015**, *53*, 100–113.
- Olasolo, P.; Juárez, M.; Morales, M. P.; D'Amico, S.; Liarte, I. A. Enhanced geothermal systems (EGS): A review. *Renew. Sustain. Energy Rev.* **2016**, *56*, 133–144.
- Yin, S.; Dusseault, M. B.; Rothenburg, L. Coupled THMC modeling of CO₂ injection by finite element methods. *J. Pet. Sci. Eng.* **2011**, *80*, 53–60.
- Zhang, F.-Z.; Jiang, P.-X.; Xu, R.-N. System thermodynamic performance comparison of CO₂-EGS and water-EGS systems. *Appl. Therm. Eng.* **2013**, *61*, 236–244.
- Garapati, N.; Randolph, J. B.; Saar, M. O. Brine displacement by CO₂, energy extraction rates, and lifespan of a CO₂-limited CO₂-Plume Geothermal (CPG) system with a horizontal production well. *Geothermics* **2015**, *55*, 182–194.
- Zhang, L.; Cui, G.; Zhang, Y.; Ren, B.; Ren, S.; Wang, X. Influence of pore water on the heat mining performance of supercritical CO₂ injected for geothermal development. *J. CO₂ Util.* **2016**, *16*, 287–300.
- Pan, C.; Romero, C. E.; Levy, E. K.; Wang, X.; Rubio-Maya, C.; Pan, L. Fully coupled wellbore-reservoir simulation of supercritical CO₂ injection from fossil fuel power plant for heat mining from geothermal reservoirs. *J. CO₂ Util.* **2018**, *27*, 480–492.
- Qu, Z.-q.; Zhang, W.; Guo, T.-k. Influence of different fracture morphology on heat mining performance of enhanced geothermal systems based on COMSOL. *Int. J. Hydrogen Energy* **2017**, *42*, 18263–18278.
- Luo, F.; Xu, R.-N.; Jiang, P.-X. Numerical investigation of fluid flow and heat transfer in a doublet enhanced geothermal system with CO₂ as the working fluid (CO₂-EGS). *Energy* **2014**, *64*, 307–322.
- Wang, C.-L.; Cheng, W.-L.; Nian, Y.-L.; Yang, L.; Han, B.-B.; Liu, M.-H. Simulation of heat extraction from CO₂-based enhanced geothermal systems considering CO₂ sequestration. *Energy* **2018**, *142*, 157–167.
- Guo, T.; Gong, F.; Wang, X.; Lin, Q.; Qu, Z.; Zhang, W. Performance of enhanced geothermal system (EGS) in fractured geothermal reservoirs with CO₂ as working fluid. *Appl. Therm. Eng.* **2019**, *152*, 215–230.
- Cheng, Y.; Zhang, Y.; Yu, Z.; Hu, Z.; Yang, Y. An investigation on hydraulic fracturing characteristics in granite geothermal reservoir. *Eng. Fract. Mech.* **2020**, *237*, 107252.
- Khoei, A.; Moallemi, S.; Haghghat, E. Thermo-hydro-mechanical modeling of impermeable discontinuity in saturated porous media with X-FEM technique. *Eng. Fract. Mech.* **2012**, *96*, 701–723.
- Huang, W.; Cao, W.; Jiang, F. Heat extraction performance of EGS with heterogeneous reservoir: A numerical evaluation. *Int. J. Heat Mass Transfer* **2017**, *108*, 645–657.
- Ranjbar, A.; Hassani, H.; Shahriar, K.; Ameri Shahrabi, M. J. Thermo-hydro-mechanical modeling of fault discontinuities using zero-thickness interface element. *J. Rock Mech. Geotech. Eng.* **2020**, *12*, 74–88.
- Teng, T.; Zhao, Y.; Gao, F.; Wang, J.; Wang, W. A fully coupled thermo-hydro-mechanical model for heat and gas transfer in thermal stimulation enhanced coal seam gas recovery. *Int. J. Heat Mass Transfer* **2018**, *125*, 866–875.
- Xin, Y.; Sun, Z.; Zhuang, L.; Yao, J.; Zhang, K.; Fan, D.; Bongole, K.; Wang, T.; Jiang, C. Numerical simulation of fluid flow and heat transfer in EGS with thermal-hydraulic-mechanical coupling method based on a rough fracture model. *Energy Procedia* **2019**, *158*, 6038–6045.
- Gan, Q.; Elsworth, D. Production optimization in fractured geothermal reservoirs by coupled discrete fracture network modeling. *Geothermics* **2016**, *62*, 131–142.
- Zeng, Y.-C.; Wu, N.-Y.; Su, Z.; Wang, X.-X.; Hu, J. Numerical simulation of heat production potential from hot dry rock by water circulating through a novel single vertical fracture at Desert Peak geothermal field. *Energy* **2013**, *63*, 268–282.
- Fox, D. B.; Sutter, D.; Beckers, K. F.; Lukawski, M. Z.; Koch, D. L.; Anderson, B. J.; Tester, J. W. Sustainable heat farming: Modeling extraction and recovery in discretely fractured geothermal reservoirs. *Geothermics* **2013**, *46*, 42–54.
- Suzuki, A.; Fomin, S. A.; Chugunov, V. A.; Niibori, Y.; Hashida, T. Fractional diffusion modeling of heat transfer in porous and fractured media. *Int. J. Heat Mass Transfer* **2016**, *103*, 611–618.
- Pandey, S.; Vishal, V. Sensitivity analysis of coupled processes and parameters on the performance of enhanced geothermal systems. *Sci. Rep.* **2017**, *7*, 17057.
- Gholizadeh Doonechaly, N.; Abdel Azim, R. R.; Rahman, S. S. A study of permeability changes due to cold fluid circulation in fractured geothermal reservoirs. *Groundwater* **2016**, *54*, 325–335.
- Gholizadeh Doonechaly, N.; Abdel Azim, R.; Rahman, S. Evaluation of recoverable energy potential from enhanced geothermal systems: a sensitivity analysis in a poro-thermo-elastic framework. *Geofluids* **2016**, *16*, 384–395.

- (32) Aliyu, M. D.; Chen, H. P. Sensitivity analysis of deep geothermal reservoir: Effect of reservoir parameters on production temperature. *Energy* **2017**, *129*, 101–113.
- (33) Ghassemi, A.; Suresh Kumar, G. Changes in fracture aperture and fluid pressure due to thermal stress and silica dissolution/precipitation induced by heat extraction from subsurface rocks. *Geothermics* **2007**, *36*, 115–140.
- (34) Aliyu, M. D.; Archer, R. A. A thermo-hydro-mechanical model of a hot dry rock geothermal reservoir. *Renewable Energy* **2021**, *176*, 475–493.
- (35) Wang, Y.; Lin, G. Efficient deep learning techniques for multiphase flow simulation in heterogeneous porous media. *J. Comput. Phys.* **2020**, *401*, 108968.
- (36) Yan, B.; Harp, D. R.; Chen, B.; Hoteit, H.; Pawar, R. J. A gradient-based deep neural network model for simulating multiphase flow in porous media. *J. Comput. Phys.* **2022**, *463*, 111277.
- (37) Yan, B.; Chen, B.; Robert Harp, D.; Jia, W.; Pawar, R. J. A robust deep learning workflow to predict multiphase flow behavior during geological CO₂ sequestration injection and Post-Injection periods. *J. Hydrol.* **2022**, *607*, 127542.
- (38) Yan, B.; Harp, D. R.; Chen, B.; Pawar, R. A physics-constrained deep learning model for simulating multiphase flow in 3D heterogeneous porous media. *Fuel* **2022**, *313*, 122693.
- (39) Tariq, Z.; Aljawad, M. S.; Hasan, A.; Murtaza, M.; Mohammed, E.; El-Husseiny, A.; Alarifi, S. A.; Mahmoud, M.; Abdulaheem, A. A systematic review of data science and machine learning applications to the oil and gas industry. *J. Pet. Explor. Prod. Technol.* **2021**, *11*, 4339–4374.
- (40) Hoteit, H.; He, X.; Yan, B.; Vahrenkamp, V. Uncertainty quantification and optimization method applied to time-continuous geothermal energy extraction. *Geothermics* **2023**, *110*, 102675.
- (41) Aminian, K.; Ameri, S.; Oyerokun, A.; Thomas, B. Prediction of flow units and permeability using artificial neural networks. *SPE Western Regional/AAPG Pacific Section Joint Meeting*; OnePetro, 2003.
- (42) Gholami, R.; Moradzadeh, A.; Maleki, S.; Amiri, S.; Hanachi, J. Applications of artificial intelligence methods in prediction of permeability in hydrocarbon reservoirs. *J. Pet. Sci. Eng.* **2014**, *122*, 643–656.
- (43) Olayiwola, T.; Tariq, Z.; Abdulaheem, A.; Mahmoud, M. Evolving strategies for shear wave velocity estimation: smart and ensemble modeling approach. *Neural. Comput. Appl.* **2021**, *33*, 17147–17159.
- (44) Elkhatatny, S.; Mahmoud, M.; Tariq, Z.; Abdulaheem, A. New insights into the prediction of heterogeneous carbonate reservoir permeability from well logs using artificial intelligence network. *Neural. Comput. Appl.* **2018**, *30*, 2673–2683.
- (45) Tariq, Z.; Mahmoud, M.; Abdulaheem, A. An intelligent data-driven model for Dean–Stark water saturation prediction in carbonate rocks. *Neural. Comput. Appl.* **2020**, *32*, 11919–11935.
- (46) Adibifard, M.; Tabatabaei-Nejad, S.; Khodapanah, E. Artificial Neural Network (ANN) to estimate reservoir parameters in Naturally Fractured Reservoirs using well test data. *J. Pet. Sci. Eng.* **2014**, *122*, 585–594.
- (47) Xue, Y.; Cheng, L.; Mou, J.; Zhao, W. A new fracture prediction method by combining genetic algorithm with neural network in low-permeability reservoirs. *J. Pet. Sci. Eng.* **2014**, *121*, 159–166.
- (48) Tahmasebi, P.; Hezarkhani, A. A fast and independent architecture of artificial neural network for permeability prediction. *J. Pet. Sci. Eng.* **2012**, *86–87*, 118–126.
- (49) Saemi, M.; Ahmadi, M.; Varjani, A. Y. Design of neural networks using genetic algorithm for the permeability estimation of the reservoir. *J. Pet. Sci. Eng.* **2007**, *59*, 97–105.
- (50) Gudala, M.; Govindarajan, S. K. Numerical investigations on a geothermal reservoir using fully coupled thermo-hydro-geomechanics with integrated RSM-machine learning and ARIMA models. *Geothermics* **2021**, *96*, 102174.
- (51) Tariq, Z.; Murtaza, M.; Mahmoud, M.; Aljawad, M. S.; Kamal, M. S. Machine learning approach to predict the dynamic linear swelling of shales treated with different waterbased drilling fluids. *Fuel* **2022**, *315*, 123282.
- (52) Desouky, M.; Tariq, Z.; Aljawad, M. S.; Alhoori, H.; Mahmoud, M.; Abdulaheem, A. Machine learning-based propped fracture conductivity correlations of several shale formations. *ACS Omega* **2021**, *6*, 18782–18792.
- (53) Tariq, Z.; Abdulaheem, A.; Mahmoud, M.; Ahmed, A. Borehole Resistivity Measurement Modeling Using Machine-Learning Techniques. *Petrophysics-The SPWLA Journal of Formation Evaluation and Reservoir Description*; SPWLA, 2018; Vol. 59, pp 761–777.
- (54) Tariq, Z.; Mahmoud, M.; Abdulaheem, A. Core log integration: a hybrid intelligent data-driven solution to improve elastic parameter prediction. *Neural. Comput. Appl.* **2019**, *31*, 8561–8581.
- (55) Yan, B.; Gudala, M.; Sun, S. Robust optimization of geothermal recovery based on a generalized thermal decline model and deep learning. *Energy Convers. Manage.* **2023**, *286*, 117033.
- (56) Yan, B.; Xu, Z.; Gudala, M.; Tariq, Z.; Finkbeiner, T. *Reservoir Modeling and Optimization Based on Deep Learning with Application to Enhanced Geothermal Systems*; SPE Reservoir Characterisation and Simulation Conference and Exhibition, 2023.
- (57) Pandey, S. N.; Singh, M. Artificial neural network to predict the thermal drawdown of enhanced geothermal system. *J. Energy Resour. Technol.* **2021**, *143*, 010901.
- (58) Kalogirou, S. A.; Florides, G. A.; Pouloupatis, P. D.; Panayides, I.; Joseph-Stylianou, J.; Zomeni, Z. Artificial neural networks for the generation of geothermal maps of ground temperature at various depths by considering land configuration. *Energy* **2012**, *48*, 233–240.
- (59) Esen, H.; Inalli, M. Modelling of a vertical ground coupled heat pump system by using artificial neural networks. *Expert Syst. Appl.* **2009**, *36*, 10229–10238.
- (60) Gudmundsdottir, H.; Horne, R. N. *Prediction Modeling for Geothermal Reservoirs Using Deep Learning. 45th Workshop on Geothermal Reservoir Engineering*; Stanford University: Stanford, CA, 2020; pp 1–12.
- (61) Akın, S.; Kok, M. V.; Uraz, I. Optimization of well placement geothermal reservoirs using artificial intelligence. *Comput. Geosci.* **2010**, *36*, 776–785.
- (62) Chen, Z.; Huan, G.; Ma, Y. *Computational Methods for Multiphase flows in porous media*; SIAM, 2006.
- (63) Biot, M. A. General theory of three-dimensional consolidation. *J. Appl. Phys.* **1941**, *12*, 155–164.
- (64) Biot, M. A. Theory of elasticity and consolidation for a porous anisotropic solid. *J. Appl. Phys.* **1955**, *26*, 182–185.
- (65) Li, S.; Feng, X.-T.; Zhang, D.; Tang, H. Coupled thermo-hydro-mechanical analysis of stimulation and production for fractured geothermal reservoirs. *Appl. Energy* **2019**, *247*, 40–59.
- (66) Liu, G.; Pu, H.; Zhao, Z.; Liu, Y. Coupled thermo-hydro-mechanical modeling on well pairs in heterogeneous porous geothermal reservoirs. *Energy* **2019**, *171*, 631–653.
- (67) Guo, T.; Tang, S.; Sun, J.; Gong, F.; Liu, X.; Qu, Z.; Zhang, W. A coupled thermal-hydraulic-mechanical modeling and evaluation of geothermal extraction in the enhanced geothermal system based on analytic hierarchy process and fuzzy comprehensive evaluation. *Appl. Energy* **2020**, *258*, 113981.
- (68) Vallier, B.; Magnenet, V.; Schmittbuhl, J.; Fond, C. THM modeling of hydrothermal circulation at Rittershoffen geothermal site, France. *Geoth. Energy* **2018**, *6*, 22–26.
- (69) Freeman, T. T.; Chalaturnyk, R. J.; Bogdanov, I. I. *Fully Coupled Thermo-Hydro-Mechanical Modeling by COMSOL Multiphysics, with Applications in Reservoir Geomechanical Characterization*; COMSOL Conf, 2008, pp 9–11.
- (70) Freeman, T. T.; Chalaturnyk, R. J.; Bogdanov, I. I. *THM Modeling for Reservoir Geomechanical Applications*; Comsol Conference, 2008.
- (71) Jianxin, L. A. Porosity-Based Model for Coupled Thermal-Hydraulic-Mechanical Processes. Ph.D. thesis, The University of Western Australia, 2009.
- (72) Miller, S. A. Modeling enhanced geothermal systems and the essential nature of large-scale changes in permeability at the onset of slip. *Geofluids* **2015**, *15*, 338–349.

- (73) Touhidi-Baghini, A. Absolute permeability of McMurray formation oil sands at low confining stresses. Ph.D. thesis, University of Alberta, 1998.
- (74) Multiphysics, C. *Subsurface Flow Module User's Guide*, Version; COMSOL, 2018; Vol. 5.
- (75) Wang, Y.; Li, T.; Chen, Y.; Ma, G. A three-dimensional thermo-hydro-mechanical coupled model for enhanced geothermal systems (EGS) embedded with discrete fracture networks. *Comput. Methods Appl. Mech. Eng.* **2019**, *356*, 465–489.
- (76) Yan, B.; Mi, L.; Chai, Z.; Wang, Y.; Killough, J. E. An Enhanced Discrete Fracture Network model for multiphase flow in fractured reservoirs. *J. Pet. Sci. Eng.* **2018**, *161*, 667–682.
- (77) Mi, L.; Yan, B.; Jiang, H.; An, C.; Wang, Y.; Killough, J. An Enhanced Discrete Fracture Network model to simulate complex fracture distribution. *J. Pet. Sci. Eng.* **2017**, *156*, 484–496.
- (78) Zhang, F.; An, M.; Yan, B.; Wang, Y.; Han, Y. A novel hydro-mechanical coupled analysis for the fractured vuggy carbonate reservoirs. *Comput. Geotech.* **2019**, *106*, 68–82.
- (79) Šijačić, D.; Fokker, P. A. *Thermo-Hydro-Mechanical modeling of EGS using COMSOL Multiphysics*; Fourtieth Workshop on Geothermal Reservoir Engineering, 2015; p 52.
- (80) Lei, Q.; Gholizadeh Doonechaly, N.; Tsang, C.-F. Modelling fluid injection-induced fracture activation, damage growth, seismicity occurrence and connectivity change in naturally fractured rocks. *Int. J. Rock Mech. Min. Sci.* **2021**, *138*, 104598.
- (81) Ghassemi, A.; Zhang, Q. A transient fictitious stress boundary element method for porothermoelastic media. *Eng. Anal. Bound. Elem.* **2004**, *28*, 1363–1373.
- (82) Zhang, L.; Cui, C.; Ma, X.; Sun, Z.; Liu, F.; Zhang, K. a Fractal Discrete Fracture Network Model for History Matching of Naturally Fractured Reservoirs. *Fractals* **2019**, *27*, 1940008.
- (83) Gudala, M.; Govindarajan, S. K.; Yan, B.; Sun, S. Numerical investigations of the PUGA geothermal reservoir with multistage hydraulic fractures and well patterns using fully coupled thermo-hydro-geomechanical modeling. *Energy* **2022**, *253*, 124173.
- (84) Sanaee, R.; Oluyemi, G. F.; Hossain, M.; Oyenyin, M. *Fracture-Matrix Flow Partitioning and Cross Flow: Numerical Modeling of Laboratory Fractured Core Flood*, Milan, 10–12 October 2012; Proceedings of the 2012 COMSOL Conference, 2012.
- (85) Lepillier, B.; Daniilidis, A.; Doonechaly Gholizadeh, N.; Bruna, P.-O.; Kummerow, J.; Bruhn, D. A fracture flow permeability and stress dependency simulation applied to multi-reservoirs, multi-production scenarios analysis. *Geoth. Energy* **2019**, *7*, 24.
- (86) Norouzi, M.; Dorrani, S.; Shokri, H.; Anwar Bég, O. Effects of viscous dissipation on miscible thermo-viscous fingering instability in porous media. *Int. J. Heat Mass Transfer* **2019**, *129*, 212–223.
- (87) Gudala, M.; Govindarajan, S. K. Numerical modelling of coupled single-phase fluid flow and geomechanics in a fractured porous media. *J. Pet. Sci. Eng.* **2020**, *191*, 107215.
- (88) Gudala, M.; Govindarajan, S. K. Numerical modeling of coupled fluid flow and geomechanical stresses in a petroleum reservoir. *J. Energy Resour. Technol.* **2020**, *142*, 063006.
- (89) Gudala, M.; Govindarajan, S. K. Numerical investigations on two-phase fluid flow in a fractured porous medium fully coupled with geomechanics. *J. Pet. Sci. Eng.* **2021**, *199*, 108328.
- (90) Bowden, G. J.; Dandy, G. C.; Maier, H. R. Input determination for neural network models in water resources applications. Part 1—background and methodology. *J. Hydrol.* **2005**, *301*, 75–92.
- (91) Bowden, G. J.; Maier, H. R.; Dandy, G. C. Input determination for neural network models in water resources applications. Part 2. Case study: forecasting salinity in a river. *J. Hydrol.* **2005**, *301*, 93–107.
- (92) Demšar, J.; Curk, T.; Erjavec, A.; Gorup, C.; Hočevar, T.; Milutinović, M.; Možina, M.; Polajnar, M.; Toplak, M.; Starič, A.; et al. Orange: data mining toolbox in Python. *J. Mach. Learn. Res.* **2013**, *14*, 2349–2353.
- (93) Lauwerier, H. The transport of heat in an oil layer caused by the injection of hot fluid. *Appl. Sci. Res., Sect. A* **1955**, *5*, 145–150.
- (94) Han, S.; Cheng, Y.; Gao, Q.; Yan, C.; Han, Z.; Zhang, J. Investigation on heat extraction characteristics in randomly fractured geothermal reservoirs considering thermo-poroelastic effects. *Energy Sci. Eng.* **2019**, *7*, 1705–1726.
- (95) Yan, B.; Harp, D. R.; Chen, B.; Hoteit, H.; Pawar, R. J. A gradient-based deep neural network model for simulating multiphase flow in porous media. *J. Comput. Phys.* **2022**, *463*, 111277.